AN EXACT DIAGONALIZATION STUDY OF A RAPIDLY ROTATING BOSE-BOSE MIXTURE WITH ATTRACTIVE INTERACTIONS

A THESIS SUBMITTED TO
THE GRADUATE SCHOOL OF NATURAL AND APPLIED SCIENCES
OF
MIDDLE EAST TECHNICAL UNIVERSITY

BY

UMUT CAN TURHAN

IN PARTIAL FULFILLMENT OF THE REQUIREMENTS
FOR
THE DEGREE OF MASTER OF SCIENCE
IN
PHYSICS

JULY 2025

Approval of the thesis:

AN EXACT DIAGONALIZATION STUDY OF A RAPIDLY ROTATING BOSE-BOSE MIXTURE WITH ATTRACTIVE INTERACTIONS

submitted by **UMUT CAN TURHAN** in partial fulfillment of the requirements for the degree of **Master of Science in Physics Department, Middle East Technical University** by,

Prof. Dr. Naci Emre ALTUN
Dean, Graduate School of **Natural and Applied Sciences** _____

Prof. Dr. Seçkin KÜRKÇÜOĞLU
Head of Department, **Physics** _____

Assist. Prof. Dr. Ahmet Keleş
Supervisor, **Physics, METU** _____

Examining Committee Members:

Prof. Dr. Mehmet Özgür Oktel
Physics, Bilkent University _____

Assist. Prof. Dr. Ahmet Keleş
Physics, METU _____

Prof. Dr. Sadi Turgut
Physics, METU _____

Prof. Dr. Rifat Onur Umucalılar
Physics, Mimar Sinan Fine Arts University _____

Prof. Dr. Bayram Tekin
Physics, METU _____

Date:23.07.2025

I hereby declare that all information in this document has been obtained and presented in accordance with academic rules and ethical conduct. I also declare that, as required by these rules and conduct, I have fully cited and referenced all material and results that are not original to this work.

Name, Surname: Umut Can Turhan

Signature :

ABSTRACT

AN EXACT DIAGONALIZATION STUDY OF A RAPIDLY ROTATING BOSE-BOSE MIXTURE WITH ATTRACTIVE INTERACTIONS

Turhan, Umut Can
M.S., Department of Physics
Supervisor: Assist. Prof. Dr. Ahmet Keleş

July 2025, 75 pages

The Hall experiment can be explained by classical transport theory for lower magnetic fields ($B \lesssim 1$ T). In Chapter 1 of this thesis, we review the Drude model to obtain cyclotron motion and to derive the conductivity tensor $\boldsymbol{\sigma}$ as a function of the magnetic field $\boldsymbol{B}$.

The quantum version of the classical Hall effect initiated a remarkable era in the search for new topological phases of two-dimensional materials and strongly correlated phases, treated via Landau quantization, which generates highly degenerate energy levels known as Landau levels (LLs). Strong, uniform magnetic fields lead to the quantization of the Hall resistivity $\rho_H = h/(e^2\nu)$, where ν is the filling fraction of electrons, taking integer or fractional values depending on the system. This quantization reflects the presence of fully and partially filled LLs. Chapter 2 addresses the role of uniform magnetic and electric fields in a 2D system by choosing an appropriate vector potential $\boldsymbol{A}$ gauge. Also, we investigate the quantum mechanical current operator that allows us to quantize the conductivity tensor element $\sigma_{xy} = e^2\nu/h$. Subsequent sections present the derivations of the wave functions in both Landau and symmetric gauges and the corresponding eigenvalues. In the final sections of Chap-

ter 2, we discuss the percolation concept, which explains Hall plateaux, and examine the role of edge states and random impurities in Hall samples by introducing confinement and random electrostatic potentials, which lead to backscattering effects at the boundaries and localized states in the bulk.

Many-body physics plays a crucial role in the partially filled LL, highlighting the strong interactions between electrons in the context of the Fractional Quantum Hall Effect (FQHE). Chapter 3 begins with an exact solution for the two-body problem at filling fraction $\nu = 1$. Laughlin's ansatz offers an elegant solution for the many-body problem at filling fraction $\nu = 1/m$, where m is even for bosons and odd for fermions. We review Laughlin's incompressible wave function, which is an essentially exact solution for short-range interactions, and discuss the plasma analogy, which describes the Laughlin state as a quantum droplet with uniform density. The last section of Chapter 3 addresses the Haldane pseudopotential, which characterizes strong interactions in the FQHE regime.

Rotating and trapped bosonic condensates exhibit unique properties for strongly correlated states in the FQHE regime, where the ground state lies in the lowest LL. The effective magnetic field generated by the Coriolis force mimics that of Quantum Hall (QH) systems, enabling the emergence of incompressible states for neutral bosons. In Chapter 4, we also study a three-dimensional rotating BEC in a harmonic trap, highlighting the connection between the FQHE and rapidly rotating BECs.

In the final chapter, we investigate an equal-number binary bosonic gas with a fixed total angular momentum L in the z-direction. The tunable coupling ratio g_{12}/g allows us to identify a critical threshold beyond which the gas becomes unstable in the strongly attractive inter-species interaction regime in disc geometry. The collapse mode refers to the instability in which the binary gas undergoes spatial contraction. Overlap calculations for the ground state show that the Laughlin square wave function, which describes two species via separate Laughlin states, vanishes near the critical coupling ratio $g_{12}/g \sim -1$, as expected. We introduce a molecular Laughlin ansatz that describes center-of-mass pairing between inter-species particles. Our molecular ansatz yields higher overlaps with both the ground state and low-lying excited states compared to the Laughlin square wave function. We also confirm that

the ground state of the gas in this regime corresponds to a collapse mode, where the system rotates around its common center of mass. The dependence of the energy spectrum on g_{12}/g and the corresponding real-space density profiles are also presented.

Keywords: Quantum Hall Systems, Strongly Correlated States, Bose-Einstein Condensate, Rotated 2D Bosonic Gas, Two Component Bosonic Gas.

ÖZ

ÇEKİCİ ETKİLEŞİMLİ, HIZLA DÖNEN BİR BOSE-BOSE KARIŞIMININ TAM KÖŞEGENLEŞTİRME YÖNTEMİYLE İNCELENMESİ

Turhan, Umut Can
Yüksek Lisans, Fizik Bölümü
Tez Yöneticisi: Dr. Öğr. Üyesi. Ahmet Keleş

Temmuz 2025 , 75 sayfa

Hall deneyi, düşük manyetik alanlar ($B \lesssim 1\mathrm{T}$) için klasik taşınım teorisi ile açıklanabilir. Bu tezin Birinci Bölümünde, Drude modeli incelenerek siklotron hareketi elde edilmiş ve iletkenlik tensörü $\boldsymbol{\sigma}$'nın manyetik alan $\boldsymbol{B}$'ye bağlılığı türetilmiştir.

Klasik Hall etkisinin kuantum versiyonu, iki boyutlu malzemelerde yeni topolojik fazların ve güçlü korelasyonlu fazların araştırılmasında dikkat çekici bir dönemi başlatmıştır. Bu fazlar, Landau kuantizasyonu ile tanımlanan ve Landau seviyeleri (LL) olarak bilinen yüksek derecede dejenereli enerji düzeyleri ile ortaya çıkar. Güçlü ve düzgün manyetik alanlar, Hall özdirencinin $\rho_H = h/(e^2\nu)$ şeklinde kuantalanmasına yol açar; burada ν, sistemin özelliğine bağlı olarak tamsayı veya kesirli değerler alabilen doluluk oranıdır. Bu kuantalanma, tamamen veya kısmen dolu LL'lerin varlığını yansıtır. İkinci Bölümde, iki boyutlu bir sistemde düzgün manyetik ve elektrik alanların rolü, uygun bir vektör potansiyeli $\boldsymbol{A}$ seçilerek ele alınmıştır. Ayrıca, iletkenlik tensörü elemanı σ_{xy}'nin kuantalanmasını sağlayan kuantum mekaniksel akım operatörü incelenmiştir. Sonraki kısımlarda, hem Landau hem de simetrik ölçekte dalga fonksiyonlarının ve karşılık gelen özdeğerlerin türetilmesi sunulmuştur. İkinci Bölü-

mün son kısmında ise Hall platosunu açıklayan perkolasyon kavramı ele alınmış; kenar durumları ve Hall örneğindeki rastgele safsızlıkların, sınır bölgelerinde saçılma ve yığın içinde lokalize durumlar oluşturmasına yol açan sınırlandırma ve rastgele elektrostatik potansiyeller aracılığıyla etkileri tartışılmıştır.

Kısmen dolu LL'lerde, elektronlar arasındaki güçlü etkileşimlerin belirleyici olduğu çok parçacıklı fizik, Kesirli Kuantum Hall Etkisi (FQHE) bağlamında kritik bir rol oynamaktadır. Üçüncü Bölüm, doluluk oranı $\nu = 1$ için iki cisim problemine ait tam çözüm ile başlar. Laughlin'in öngördüğü ansatz, doluluk oranı $\nu = 1/m$ (bosonlar için m çift, fermiyonlar için tek) olan çok parçacık problemine zarif bir çözüm sunar. Laughlin'in sıkıştırılamaz dalga fonksiyonu, kısa menzilli etkileşimler için neredeyse tam bir çözümdür. Ayrıca, Laughlin durumunu düzgün yoğunluklu bir kuantum damlacığı olarak yorumlayan plazma analojisi ve FQHE rejimindeki güçlü etkileşimleri tanımlayan Haldane psödopotansiyeli incelenmiştir.

Dönen ve tuzaklanmış bozonik yoğuşuklar, temel durumun en düşük LL'de yer aldığı FQHE rejiminde benzersiz özellikler sergiler. Coriolis kuvveti tarafından üretilen efektif manyetik alan, Kuantum Hall (QH) sistemlerini taklit ederek yüksüz bozonlar için sıkıştırılamaz durumların ortaya çıkmasına imkân tanır. Dördüncü bölümde ayrıca, harmonik tuzakta üç boyutlu dönen bir BEC incelenmiş ve FQHE ile hızlı dönen BEC'ler arasındaki bağlantı vurgulanmıştır.

Son bölümde, toplam açısal momentumu z-yönünde sabit olan, eşit sayıda parçacıktan oluşan iki bileşenli bozonik gaz sistemi incelenmiştir. Ayarlanabilir etkileşim oranı g_{12}/g, disk geometrisinde güçlü çekici türler arası etkileşim bölgesinde gazın kararsız hale geldiği kritik eşiğin belirlenmesini sağlamaktadır. Çökme modu, ikili gazın uzaysal olarak daralması ile karakterize edilen bir kararsızlık durumudur. Temel durum için yapılan örtüşme hesaplamaları, iki türü ayrı Laughlin durumları ile tanımlayan Laughlin kare dalga fonksiyonunun, $g_{12}/g \sim -1$ kritik oranına yaklaşırken kaybolduğunu göstermektedir. Türler arası parçacıklar arasında kütle merkezi eşleşmesini tanımlayan moleküler Laughlin ansatz'ı önerilmiştir. Bu moleküler ansatz, hem temel durum hem de uyarılmış durumlar için Laughlin kare dalga fonksiyonuna kıyasla daha yüksek örtüşme sağlamaktadır. Ayrıca, bu rejimde gazın ortak kütle merkezi etrafında döndüğü bir çökme modunda temel durum oluşturduğunu doğrulamak-

tayız. Enerji spektrumunun g_{12}/g'ye bağlılığı ve karşılık gelen gerçek uzay yoğunluk profilleri de sunulmuştur.

Anahtar Kelimeler: Kuantum Hall Sistemleri, Güçlü İlintili Kuantum Durumları, Bose-Einstein Yoğuşması, 2 Boyutlu Dönen Gaz, İki Bileşenli Boson Gazı.

I dedicate my dissertation study to my precious family. My sister Berna Mine, whose endless encouragement. My loving parents, Sait and Fatma, whose quiet strength and boundless wisdom continue to inspire every step I take.

I also dedicate this dissertation and extend special thanks to my valued friends, especially Recep Yılkıcı, for our helpful discussions; Eyyüp Emre Tan, who has always believed in me; and last but certainly not least, Özgür Nazlı, for the unwavering support.

I will always appreciate all they have done.

ACKNOWLEDGMENTS

Completing this thesis has not only been an academic challenge but also a profound journey of personal and mental growth. I want to express my deepest appreciation to my advisor, Asst. Prof. Ahmet KELEŞ, whose assistance has been invaluable, and mentorship extended beyond the academic realm into personal guidance, providing comfort and motivation during tough times.

A heartfelt thanks to my Co-Advisor, Prof. Dr. Mehmet Özgür OKTEL, for sharing his deep scientific insights and offering insightful advice throughout this thesis. I could not have undertaken this journey without Prof. Dr. Rifat Onur UMUCALILAR, whose indispensable assistance and support have been constant since my undergraduate days. His intellectual rigor and constructive feedback not only shaped this research but also fostered my growth as a scholar. Thank you for your patience, your time, and for consistently inspiring me to push the boundaries of my understanding.

I extend heartfelt thanks to my lifelong mentor, Prof. Dr. Ahmet Levent SUBAŞI, for his dedicated support and guidance that enabled me to adapt to challenging research problems. I owe an immense debt of gratitude to him.

I am equally thankful to the members of my thesis committee, Sadi TURGUT and Bayram TEKİN, for their constructive feedback and essential suggestions that enhanced the quality of my work. To all those who contributed in any way to this thesis, I extend my sincere thanks. Finally, I would like to acknowledge the TÜBİTAK (Scientific and Technological Research Council of Türkiye) for providing the resources that made this research possible.

As a final word, this journey constantly reminded me that the pursuit of science is a demanding, time-intensive mental undertaking. This is precisely why learning and leaving our teachings as a legacy for future generations is the world's most challenging yet priceless treasure. We must always raise individuals who are aware of this. We should illuminate our path with the joy of scientific discovery.

May you learn and teach throughout your lives; stay well and dedicated to science, with my regards...

Umut Can Turhan

24/06/2025

TABLE OF CONTENTS

ABSTRACT v

ÖZ viii

ACKNOWLEDGMENTS xii

TABLE OF CONTENTS xiv

LIST OF TABLES xvii

LIST OF FIGURES xviii

LIST OF ABBREVIATIONS xxii

CHAPTERS

1 CLASSIC HALL EFFECT 1

1.1 Introduction 1

1.2 2D Motion of a Charged Particle in a Uniform Magnetic Field 1

1.3 The Drude Model 3

2 INTEGER QUANTUM HALL EFFECT 7

2.1 Introduction 7

2.2 Classical Mechanics 7

2.2.1 Lagrangian 8

2.2.2 Hamiltonian 9

2.3 Landau Levels 9

2.4 Quantization in the Landau Gauge 10
2.5 The Number of the Degeneracy in the Landau Levels 11
2.6 The Role of Uniform Electric Field 13
2.7 Quantization in the Symmetric Gauge 14
2.8 Treatment of Conductivity 16
2.8.1 $\boldsymbol{E} \times \boldsymbol{B}$ Drift 18
2.9 Edge States 19
2.10 Disorder & Percolation 22
3 FRACTIONAL QUANTUM HALL EFFECT 27
3.1 Introduction 27
3.2 Two-Body Problem 28
3.3 Many-Body Problem 30
3.4 Laughlin Wave Function 31
3.4.1 Plasma Analogy 31
3.5 Haldane Pseudopotential 33
4 ROTATING BEC IN 2D PLANE 37
4.1 Introduction 37
4.2 The Role of Superfluidity Under the Rotation 40
4.3 Rotating Frame of Reference 41
4.4 Eigenvalues 42
4.5 Rapidly Rotating BEC 44
5 BINARY BOSONIC GAS IN RAPIDLY ROTATING LIMIT 47
5.1 Introduction 47

5.2 Binary Bosonic Gas 48
5.3 Numerical Analysis 49
5.3.1 Energy Spectrum 50
5.3.2 Stability of Bosonic Mixtures 51
5.3.2.1 Overlap Study 54
5.3.2.2 Energy Gap Study 56
5.3.3 A Novel Ansatz: Molecular Laughlin 57
5.3.4 Higher Excited States 59
5.3.5 Real-Space Profile 61
6 CONCLUSION 63

LIST OF TABLES

TABLES

Table 5.1 The Hilbert space dimensions $\mathcal{D}$ for the numeric parameters that we used in this thesis. 50

LIST OF FIGURES

FIGURES

Figure 1.1 A schematic representation of the 2D experimental setup for measurement of the Hall voltage V_H. This figure is adapted from [2]. . . 2

Figure 1.2 The cyclotron motion of the electron in the 2D (x-y plane) for the opposite directions of the magnetic field $\boldsymbol{B}$ in the z-direction. 3

Figure 1.3 Longitudinal (DC resistivity) ρ_{xx} and Hall (transverse) ρ_H resistivities as a function of magnetic field B are given by Equation (1.17). This figure is adapted from [7]. 4

Figure 2.1 The experimental evidence of the IQHE. We see the results of the CHE (1.17) for the lower magnetic field regime. As the magnetic field increases, the Hall plateaux appear in the Hall resistivity ρ_H (blue lines), which is shown as ρ_{xy} in the figure, at integer ν values (black lines), meanwhile, ρ_{xx} having zero value (red lines). This figure is taken from [13]. 8

Figure 2.2 The degenerate LLs of the charged particle under the uniform magnetic field. The integers represent the LL indices n. This figure is adapted from [9]. 12

Figure 2.3 The dispersion relation of the confinement model. The Fermi level, represented by a horizontal green-dashed line. The band of the bulk is degenerate LLs, which are labeled by n, but due to the effect of the confinement potential, the degeneracy is lifted smoothly on the edges, resulting in bending energy levels. This figure is adapted from [4] 20

Figure 2.4 Cylotron orbits under the uniform magnetic field. The full cyclotron motion corresponds to the states that are described by the LL energies in the bulk. The half-cyclotron orbits represent the edge motion that moves along the x-direction due to the non-zero drift velocity. This figure is adapted from [16]. 21

Figure 2.5 A schematic representation of the electrostatic potential landscape due to the random impurities. The current flows through the sample due to the potential difference $\Delta\mu = \mu_R - \mu_L$. The blue lines indicate the equipotential regions that are created by the positive and negative impurities. The red arrows indicate the cyclotron motion, which is constrained by the equipotential lines. The equipotential lines become straight near the edge due to the confinement potential in the x-direction. This figure is adapted from [2]. 22

Figure 2.6 Density of states $D(\mathcal{E})$ for a 2D electron gas as a function of energies $\mathcal{E}$. (A) If there is no magnetic field in the system, we have a constant density of states. (B) If there is a magnetic field in the ideal (pure) system, the density of states shows peaks at LLs. (C) If there is a magnetic field in the system that has an impurity, we see broadened density of states where localised(gray shaded areas) and extended states (white areas) occur. This figure is adapted from [9]. 24

Figure 2.7 Representation of the percolation on the Hall bar. The first row shows the impurity broadened density of states, where the blue dashed line represents the Fermi energy ϵ_F, and LLs are labeled by n. The second row shows the percolation steps on the Hall bar, where the purple area indicates the electron density at potential difference $\Delta\mu$. The last row shows the Hall plateaux, where ρ_H and ρ_{xx} are the Hall and longitudinal resistivities, respectively. This figure is adapted from [2]. . 25

Figure 3.1 The number of degeneracies on each LLs (Equation 3.2) making problem hard to solve analytically. 29

Figure 5.1 The low-lying energy E spectrum of the two-component rapidly rotating bosonic gas as a function of total angular momentum L in the range of $35 \leq L \leq 45$. The calculations are performed for a system of $N = 5 + 5$ particles with an angular momentum-cutoff of $M = 9$ and the coupling ratio is fixed at $g_{12}/g = 0$. 52

Figure 5.2 The low-lying energy E spectrum of the two-component rapidly rotating bosonic gas as a function of total angular momentum L in the range of $35 \leq L \leq 45$. The calculations are performed for a system of $N = 5 + 5$ particles with an angular momentum-cutoff of $M = 9$, and the coupling ratio is fixed at $g_{12}/g = -1.1$, which is below the threshold value. 53

Figure 5.3 The overlap square $\mathcal{F}$ between the exact ground and analytic collapse state (5.13) as a funtion of coupling ratio g_{12}/g for three different particle sector: $N = \{2 + 2, 3 + 3\}$ and $N = 4 + 4$ are represented by blue circle, orange star and green square, respectively. To ensure that the basis is large enough to accurately describe the Laughlin square state and its potential transition to a collapse state, we use an angular momentum cutoff M equal to the total angular momentum of the Laughlin square state, $L = 2N(N - 1)$, at filling fraction $\nu = 1/2$. . 54

Figure 5.4 The overlap square $\mathcal{F}$ between the exact ground and analytic Laughlin square state (5.8) as a function of coupling ratio g_{12}/g for three different particle sector: $N = \{2 + 2, 3 + 3\}$ and $N = 4 + 4$ are represented by blue circle, orange star and green square, respectively. The data for the parameter set $N = 5 + 5, M = 8, L = 40$ is the same as the figure (5.1). 55

Figure 5.5 Eigenvalues of ground (blue line) and first excited (orange line) states as a function of coupling ratio g_{12}/g for $N = 5{+}5$ in the Laughlin square regime $M = 8, L = 40$. Level crossing occurs at the critical threshold value, indicated by a gray dashed vertical line at $g_{12}/g = -1.003$. 57

Figure 5.6 The ground state overlap $\mathcal{F}$ as a function of coupling ratio g_{12}/g for the Lauglin square (solid lines) and molecular ansatz (dashed lines) for the particle sectors $N = \{2+2, 3+3, 4+4\}$, blue, red, and green colors, respectively. The black dot symbols represent the intersection. The angular momentum cut-off is fixed by $M = 2m(N-1)$, where $m = 2$ for the one-half filling fraction Laughlin square. 59

Figure 5.7 The sorted n eigenvalues E (left panel) and molecular ansatz overlap squares $\mathcal{F}$ as a function of eigenvalues (right panel) of the parameter space $N = 4+4$, $M = 12$ and $L = 24$. The red dots show the states that have relatively higher overlaps between $k = 65$ low-lying eigenstates. The coupling ratio is fixed at $g_{12}/g = -1.027$. The limits have been set for the x-axis on the right panel to show the quasi-degenerate band states. 60

Figure 5.8 Molecular ansatz overlaps for the low-lying higher excited states as a function of bandwidth δE for the parameter set $N = 4+4, M = 12, L = 24$. We fixed the coupling ratio at $g_{12}/g = -1.027$. 61

Figure 5.9 Real-space one species density of the ground state for attractive interaction $g_{12}/g = 0$, repulsive for the just before $g_{12}/g = -1.002$, and at the collapse critical threshold $g_{12}/g = -1.003$, respectively. The second row of the figure shows the one-dimensional cut of the first row, and the parameter set is $N = 5+5, M = 8, L = 40$. 62

LIST OF ABBREVIATIONS

2D	2 Dimensional
3D	3 Dimensional
IQHE	Integer Quantum Hall Effect
MB	Many-Body
FQHE	Fractional Quantum Hall Effect
LLs	Landau Levels
LLL	Lowest Landau Level
B, E	Magnetic and Electric Fields
$\boldsymbol{\sigma}, \boldsymbol{\rho}$	Conductivity and Resistivity Tensors
ρ_{ii}, ρ_{ij}	Longitudinal and Transverse Resistivity
ν	Filling Fraction
$\rho_H = \frac{h}{e^2}\frac{1}{\nu}$	Hall resistivity
R_K	Klitzing Constant
$l_B = \sqrt{\frac{\hbar}{eB}}$	Magnetic Length
$\omega_B = \frac{eB}{m}$	Cyclotron Frequency
Φ_0	Flux Quanta
N_Φ	The Number of Magnetic Flux Quanta

CHAPTER 1

CLASSIC HALL EFFECT

1.1 Introduction

The Classical Hall effect (CHE) was discovered by *Edwin H. Hall* in 1879 [1]. The setup consists of a uniform magnetic field $\boldsymbol{B}$ along the z-direction and perpendicular to the sample, with length L in the x-direction and width W in the y-direction (Figure 1.1). There is an electric field E_x, which is generated from a power source. So, the magnetic field $\boldsymbol{B}$ creates the Lorentz force F_B, resulting in charges deflecting towards one edge of the sample and negative charges towards the opposite edge. This effect leads to a new electric field E_y that appears in the y-direction because of the electrons that are accumulated into two distinct edges of the sample. The existence of the new transverse electric field E_y leads to the measurement of a new quantity called *Hall Voltage* V_H.

1.2 2D Motion of a Charged Particle in a Uniform Magnetic Field

The CHE arises from the fact that the magnetic field affects the charged particles in the sample. The magnetic force $\boldsymbol{F}_B$ on the particles equals the Lorentz force [3][4], governing the equation of motion from Newton's second law as follows,

$$\boldsymbol{F}_B = q\boldsymbol{v} \times \boldsymbol{B}, \tag{1.1}$$

where $q = -e$ is the charge of an electron. Consider the magnetic field $\boldsymbol{B} = B\hat{z}$ is perpendicular to the x-y plane, where the electrons move, resulting in $\boldsymbol{v} \times \boldsymbol{B} = B(\dot{y}\hat{x} - \dot{x}\hat{y})$. The equation of motion (1.1) turns out to be,

$$m\ddot{x} = -eB\dot{y}, \quad m\ddot{y} = eB\dot{x}, \tag{1.2}$$

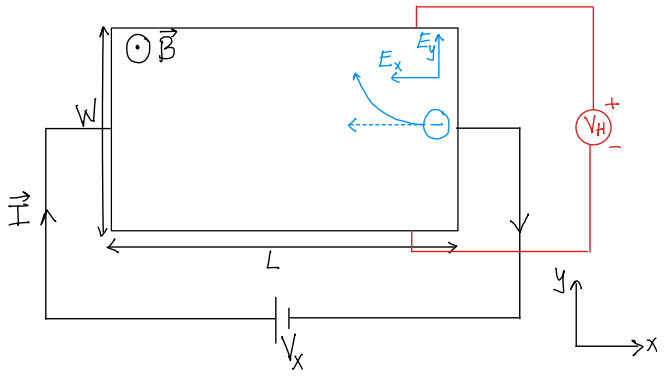

Figure 1.1: A schematic representation of the 2D experimental setup for measurement of the Hall voltage V_H. This figure is adapted from [2].

where $\ddot{x} = d^2x/dt^2$. To solve a coupled ordinary differential equation, one can start with the first equation of (1.2) by differentiating, which results in $\ddot{v}_x + w_B^2 v_x = 0$, where $w_B = eB/m$ is the cyclotron frequency and $v_x = \dot{x}$. It is a second-order harmonic oscillator equation, with a general solution,

$$v_x(t) = \dot{x}(t) = v_0 \cos(w_B t + \phi), \tag{1.3}$$

where v_0 and ϕ are real constants. The term $\dot{y}$ can be solved from the first equation of (1.2) by using the $\dot{x}$ variable in the Equation (1.3). We have,

$$\dot{y} = v_0 \sin(\omega_B t + \phi). \tag{1.4}$$

Integrating the above equation yields,

$$y(t) = -R\cos(\omega_B t + \phi) + Y, \tag{1.5}$$

where Y is an integration constant and $R = v_0/\omega_B$ is the radius of the motion. On the other hand, one can solve for the $x(t)$ from (1.3), which reads,

$$x(t) = R\sin(\omega_B t + \phi) + X, \tag{1.6}$$

where X is an integration constant. As seen in the solutions for $x(t)$ and $y(t)$, the charged particle moves in an anti-clockwise direction in a circle with radius R for $B > 0$, called a *cyclotron orbit*. As the direction of the magnetic field is changed to $B < 0$, the particle moves in the form of a clockwise cyclotron orbit (Figure 1.2).

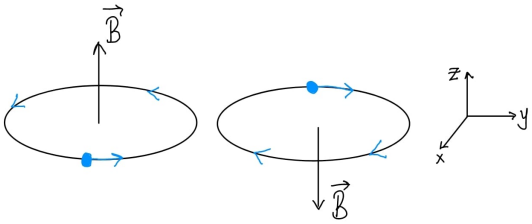

Figure 1.2: The cyclotron motion of the electron in the 2D (x-y plane) for the opposite directions of the magnetic field $\boldsymbol{B}$ in the z-direction.

While the motion of an electron in a uniform magnetic field is described by a cyclotron orbit (Figure 1.2), the case within a real sample is more complex. Inside the sample, electrons are not only subject to the magnetic field but also to an applied electric field $\boldsymbol{E}$ and, more importantly, to collisions with the immobile particles. To get this more realistic model, we will consider the Drude model in the next sub-chapter.

1.3 The Drude Model

The Drude model explains the transport properties of electrons in a material by considering electrons interacting with immobile particles (i.e., crystal ions, lattices) in the presence of uniform electric $\boldsymbol{E}$ and magnetic fields $\boldsymbol{B}$ [5, 6]. The equation of motion that governs the Drude model is given by,

$$m\frac{d\boldsymbol{v}}{dt} = \boldsymbol{F}_B - \frac{\boldsymbol{p}}{\tau}. \tag{1.7}$$

where $\boldsymbol{F}_B = -e(\boldsymbol{E} + \boldsymbol{v} \times \boldsymbol{B})$ is the Lorentz force, $\boldsymbol{p} = m\boldsymbol{v}$ is the linear momentum, and τ is the scattering time due to the collision between electrons and immobile particles. The simplest way to solve the Drude model is to assume a steady state, in which the electrons reach a constant average velocity, meaning their acceleration $(\dot{\boldsymbol{v}} = 0)$ is zero. We have,

$$-\frac{e^2 n\tau}{m}\boldsymbol{E} - \frac{e^2 n\tau}{m}\boldsymbol{v} \times \boldsymbol{B} - en\boldsymbol{v} = 0, \tag{1.8}$$

where we multiply both sides of the above equation by $en\tau/m$. After substituting the current density $\boldsymbol{J} = ne\boldsymbol{v}$, where n is the density of the electrons. One can find,

$$\begin{aligned} J_x &= \frac{e^2 n\tau}{m}\left(E_x - Bv_y\right) \\ J_y &= \frac{e^2 n\tau}{m}\left(E_x + Bv_y\right). \end{aligned} \tag{1.9}$$

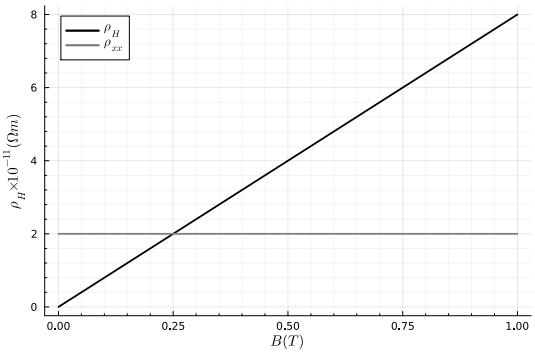

Figure 1.3: Longitudinal (DC resistivity) ρ_{xx} and Hall (transverse) ρ_H resistivities as a function of magnetic field B are given by Equation (1.17). This figure is adapted from [7].

Electric field $\boldsymbol{E}$ and current density $\boldsymbol{J}$ can be rearranged in the following way,

$$\boldsymbol{E} = \begin{pmatrix} E_x \\ E_y \end{pmatrix}, \boldsymbol{J} = \begin{pmatrix} J_x \\ J_y \end{pmatrix}. \tag{1.10}$$

Then the equation (1.9) can be written in matrix form as follows [8–10],

$$\begin{pmatrix} 1 & \omega_B\tau \\ -\omega_B\tau & 1 \end{pmatrix} \boldsymbol{J} = \frac{e^2 n\tau}{m}\boldsymbol{E}, \tag{1.11}$$

The Equation (1.11) is called Ohm's Law $\boldsymbol{J} = \boldsymbol{\sigma}\boldsymbol{E}$, where $\boldsymbol{\sigma}$ is the conductivity tensor. From Ohm's Law (1.11), the conductivity tensor $\boldsymbol{\sigma}$ can be found as,

$$\boldsymbol{\sigma} \equiv \begin{pmatrix} \sigma_{xx} & \sigma_{xy} \\ \sigma_{xy} & \sigma_{yy} \end{pmatrix} = \frac{\sigma_0}{(1+\omega_B^2\tau^2)} \begin{pmatrix} 1 & -\omega_B\tau \\ \omega_B\tau & 1 \end{pmatrix} \tag{1.12}$$

where the $\sigma_0 \equiv e^2 n\tau/m$ is the Drude conductivity. It is possible to define resistivity, which is the inverse of the conductivity $\boldsymbol{\rho} = \boldsymbol{\sigma}^{-1}$, as follows,

$$\boldsymbol{E} = \boldsymbol{\rho}\boldsymbol{J}, \quad \text{where } \boldsymbol{\rho} \equiv \begin{pmatrix} \rho_{xx} & \rho_{xy} \\ \rho_{xy} & \rho_{yy} \end{pmatrix} = \sigma_0^{-1} \begin{pmatrix} 1 & \omega_B\tau \\ -\omega_B\tau & 1 \end{pmatrix}. \tag{1.13}$$

The DC resistance R and resistivity ρ are related by the length of the sample, L such that [4],

$$R = \rho L^{2-d}, \tag{1.14}$$

where d is the dimension. In two dimensions ($d = 2$), the off-diagonal element of the resistivity tensor ρ_{xy}, which is known as the Hall resistivity or transverse resistivity, is equal to the transverse direct current (DC) resistance R_{xy}, such that,

$$R_{xy} = \frac{V_H}{I_x} = \frac{E_y W}{J_x W} = \frac{E_y}{J_x} = \rho_{xy}, \tag{1.15}$$

where V_H is the Hall voltage, which is measured in the y-direction. As a result, the transverse resistivity ρ_{xy} and transverse DC resistance R_{xy} have the same dimensionality in 2D.

The Hall coefficient R_H is defined as,

$$R_H \equiv \frac{E_y}{J_x B} = \frac{\rho_{xy}}{B} = \frac{1}{ne}, \tag{1.16}$$

which only depends on the microscopic properties of the sample and is independent of scattering time τ, so that it is an intrinsic material property.

In conclusion, we obtain longitudinal ρ_{xx} and Hall resistivities ρ_{xy} from the resistivity tensor (1.13):

$$\rho_{xx} = \frac{m}{ne^2\tau}, \quad \rho_{xy} = \frac{B}{ne}. \tag{1.17}$$

The Drude model indicates that Hall resistivity ρ_{xy} is linear with respect to the magnetic field, while the longitudinal resistivity ρ_{xx} remains unaffected by it (Figure 1.3).

CHAPTER 2

INTEGER QUANTUM HALL EFFECT

2.1 Introduction

The Integer Quantum Hall Effect (IQHE) was discovered by von Klitzing, Dorda, and Pepper in 1980 [11, 12]. 2D electron gas in a high magnetic field $\boldsymbol{B}$, which is perpendicular to the gas, reveals counterintuitive results after a hundred years of discovering the CHE. Contrary to the calculations of the classical Drude model (1.17), in a higher magnetic field regime, surprisingly, Hall plateaux in ρ_H become recognizable as a function of the magnetic field $\boldsymbol{B}$, which means that ρ_H is quantized (Figure 2.1) as follows,

$$\rho_H = \frac{h}{e^2}\frac{1}{\nu}, \tag{2.1}$$

where ν is a positive integer constant. The Hall plateaux appear as long as the longitudinal resistivity ρ_{xx} vanishes, and a next plateau immediately occurs where ρ_{xx} peaks between Hall plateaux (Figure 2.1).

The quantization of the Hall resistivity ρ_H is valid for all types of materials, and the value of ν is determined in the order of magnitude 10^{-9} precision. Also, h/e^2 is called the *Klitzing* constant R_K, which has been used for standard resistance since 1990,

$$R_K = \frac{h}{e^2} = 25,812,807\Omega. \tag{2.2}$$

2.2 Classical Mechanics

To understand the quantization of the Hall resistivity ρ_H, one first needs to understand the dynamics of charged particles in a uniform magnetic field.

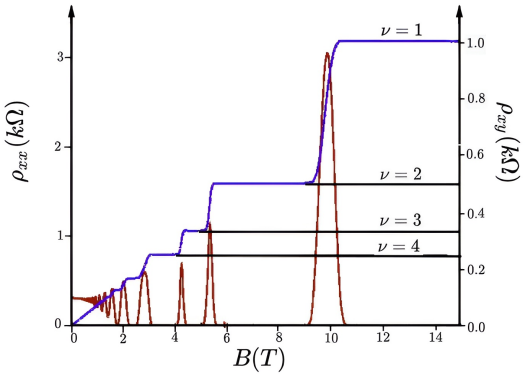

Figure 2.1: The experimental evidence of the IQHE. We see the results of the CHE (1.17) for the lower magnetic field regime. As the magnetic field increases, the Hall plateaux appear in the Hall resistivity ρ_H (blue lines), which is shown as ρ_{xy} in the figure, at integer ν values (black lines), meanwhile, ρ_{xx} having zero value (red lines). This figure is taken from [13].

2.2.1 Lagrangian

The Lagrangian of the simplest model that satisfies the Lorentz force is given by [4],

$$L = \frac{1}{2}mv^2 + q\left[\boldsymbol{v}\cdot\boldsymbol{A}(x,y,z,t) - \phi(x,y,z)\right], \quad \text{where } \boldsymbol{v} = v_x\hat{x} + v_y\hat{y} + v_z\hat{z}, \tag{2.3}$$

where ϕ is the electrostatic potential, and $\boldsymbol{A}$ is the vector potential. The Lagrangian equation of motion is given by,

$$\frac{d}{dt}\left(\frac{\partial L}{\partial v_r}\right) = \frac{\partial L}{\partial r}, \quad \text{where } r = \{x,y,z\}. \tag{2.4}$$

The Lagrange equation of motion can be decomposed into three components x, y, z. We can start with the following calculation for the x component,

$$\frac{d}{dt}\left(\frac{\partial L}{\partial v_x}\right) = \frac{d}{dt}\left(mv_x + qA_x\right) = m\frac{dv_x}{dt} + q\frac{dA_x}{dt}. \tag{2.5}$$

The total derivative for the last term of the above expression is given by,

$$\frac{dA_x}{dt} = \frac{dx}{dt}\frac{\partial A_x}{\partial x} + \frac{dy}{dt}\frac{\partial A_x}{\partial y} + \frac{dz}{dt}\frac{\partial A_x}{\partial z} + \frac{dt}{dt}\frac{\partial A_x}{\partial t}. \tag{2.6}$$

The left-hand side of the eom (2.4) becomes,

$$\frac{d}{dt}\left(\frac{\partial L}{\partial v_x}\right) = m\frac{dv_x}{dt} + \left(v_x\frac{dA_x}{dx} + v_y\frac{dA_x}{dy} + v_z\frac{dA_x}{dz} + \frac{dA_x}{dt}\right). \tag{2.7}$$

The next step is calculating the right-hand side of the eom (2.4) for the x component, which gives,

$$\frac{\partial L}{\partial x} = -q\frac{\partial \phi}{\partial x} + q\left(v_x\frac{\partial A_x}{\partial x} + v_y\frac{\partial A_y}{\partial x} + v_z\frac{\partial A_z}{\partial x}\right). \tag{2.8}$$

As a result, the eom for the x component is calculated as follows,

$$m\frac{dv_x}{dt} = -q\left[\frac{\partial \phi}{\partial x} + \frac{\partial A_x}{\partial t}\right] + q\left[v_y\left(\frac{\partial A_y}{\partial x} - \frac{\partial A_x}{\partial y}\right) + v_z\left(\frac{\partial A_z}{\partial x} - \frac{\partial A_x}{\partial z}\right)\right]. \tag{2.9}$$

As a result, we have,

$$m\frac{dv_x}{dt} = qE_x + q\left(\boldsymbol{v}\times\boldsymbol{B}\right)_x. \tag{2.10}$$

Since the contribution for the other components is the same, the Lagrangian (2.3), which describes the charged particle in the uniform magnetic field, provides the Lorentz force:

$$\boldsymbol{F}_B = q\left(\boldsymbol{E} + \boldsymbol{v}\times\boldsymbol{B}\right). \tag{2.11}$$

2.2.2 Hamiltonian

The Hamiltonian of the model can be calculated by using the Legendre transformation, which follows [4],

$$H = \dot{q}_i\frac{\partial L}{\partial \dot{q}_i} - L, \quad \text{where } q_i = \{x, y, z\}, \tag{2.12}$$

where L is the Lagrangian (2.3) that we used. The Hamiltonian becomes,

$$H = \frac{1}{2m}\left(\boldsymbol{p} + e\boldsymbol{A}\right)^2 - e\phi, \tag{2.13}$$

where we used $q \to -e$.

2.3 Landau Levels

The classical framework successfully derives the Lorentz force, which governs the dynamics of a charged particle in an electromagnetic field. However, as stated, the distinct Hall plateaus seen in experiments (2.1) cannot be understood using these classical arguments; they are a clear sign that quantum mechanics is essential. To

explain the quantization of the Hall resistivity, we must therefore transition from a classical to a quantum description.

In quantum mechanics, the Hamiltonian operator is associated with the Schrödinger equation. Consider a model in a uniform magnetic field, from the Equation (Fig. 2.13), one reads,

$$H = \frac{1}{2m}\left(\boldsymbol{p} + e\boldsymbol{A}\right)^2 \equiv \frac{\boldsymbol{\Pi}^2}{2m}, \tag{2.14}$$

where $\boldsymbol{E} = 0$, and $\boldsymbol{\Pi} = \boldsymbol{p} + e\boldsymbol{A}$ is mechanical momentum. The more convenient way to diagonalize the Hamiltonian is using the operator method. One can define the ladder operators a and $a^\dagger$ as follows,

$$a^\dagger = \frac{1}{\sqrt{2e\hbar B}}\left(\Pi_x + i\Pi_y\right), \quad a = \frac{1}{\sqrt{2e\hbar B}}\left(\Pi_x - i\Pi_y\right). \tag{2.15}$$

where $[a, a^\dagger] = 1$. The final form of the Hamiltonian becomes,

$$H = \hbar\omega_B\left(a^\dagger a + \frac{1}{2}\right), \tag{2.16}$$

where $\omega_B = eB/m$ is the cyclotron frequency. Define the number operator $N = a^\dagger a$ that satisfy the $N\left|n\right\rangle = n\left|n\right\rangle$ eigenvalue problem. Since, $[H, n] = 0$, the eigenvalues of the model (2.14) can be calculated as,

$$E_n = \hbar\omega_B\left(n + \frac{1}{2}\right). \tag{2.17}$$

These eigenvalues are called *Landau* levels (LL) [4, 9, 10, 14, 15].

2.4 Quantization in the Landau Gauge

In this chapter, we solve the Schrödinger equation for an electron that moves on a 2D plane with a uniform magnetic field in the z-direction $\boldsymbol{B} = B\hat{z}$. We choose the Landau gauge $\boldsymbol{A} = Bx\hat{y}$. The magnetic field does not change $\boldsymbol{B}$ under this gauge transformation $\boldsymbol{A} \rightarrow \boldsymbol{A}' = B\hat{z}$. The Hamiltonian (2.14) with the Landau gauge becomes,

$$H = \frac{1}{2m}p_x^2 + \frac{1}{2m}\left(p_y + eBx\right)^2. \tag{2.18}$$

The above Hamiltonian does not depend explicitly y coordinate, therefore $\dot{p}_y = -\partial H/\partial y = 0$, which results in the conservation of the mechanical momentum in

the y-direction. Now, consider a plane wave ansatz $\psi_k(x,y) = e^{iky} f_k(x)$ that satisfies the following Scrödinger equation,

$$H\psi_k(x,y) = E_n\psi_k(x,y), \tag{2.19}$$

where H is the Hamiltonian, which is given by the equation (2.18), and E_n are the LL eigenvalues (2.17). The momentum operator in the y-direction acts on the wave function as follows,

$$p_y\psi_k(x,y) = -i\hbar\frac{\partial\psi_k(x,y)}{\partial y} = \hbar k\psi_k(x,y), \tag{2.20}$$

and the Schrödinger equation will be,

$$H_k f_k(x) = E_n f_k(x), \quad \text{where } H_k = \frac{1}{2m}p_x^2 + \frac{1}{2}m\omega_B^2\left(x + kl_B^2\right)^2, \tag{2.21}$$

where H_k is nothing but a simple harmonic Hamiltonian and $l_B = \sqrt{\hbar/(eB)}$ is the magnetic length. One can use the analogy of the general wave function of the harmonic oscillator to write down the wave function in the Landau gauge as follows [9],

$$\psi_{n,k}(x,y) \propto e^{iky} H_n\left(\frac{x + kl_B^2}{l_B}\right) e^{(x+kl_B^2)^2/2l_B^2}, \tag{2.22}$$

where H_n are Hermite polynomials. Notice that we start to solve the Schrödinger equation with the ansatz $\psi_k(x,y)$, and we add sub-indices n due to the dependency that comes from Hermite polynomials H_n. The wave functions $\psi_{n,k}(x,y)$ in the Landau gauge depend on both n, k integers; meanwhile, the Landau levels (2.17) depend only on n an integer, meaning that the LL consist of degeneracy (Figure 2.2).

2.5 The Number of the Degeneracy in the Landau Levels

To calculate the number of degeneracies in the LLs (2.17), we start with the decomposition of the coordinates from the definition of mechanical momentum $\boldsymbol{\Pi} = \boldsymbol{p} + e\boldsymbol{A} = m\dot{\boldsymbol{x}}$ and pseudo-momentum $\tilde{\boldsymbol{\Pi}} = \boldsymbol{p} - e\boldsymbol{A}$ operators in the symmetric gauge $\boldsymbol{A} = \frac{eB}{2}(-y, x, 0)$ as follows,

$$\begin{aligned} x &= \frac{1}{eB}\left(\Pi_y - \tilde{\Pi}_x\right) \\ y &= \frac{1}{eB}\left(\tilde{\Pi}_x - \Pi_x\right). \end{aligned} \tag{2.23}$$

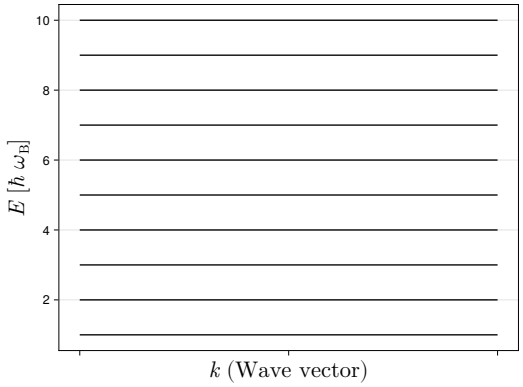

Figure 2.2: The degenerate LLs of the charged particle under the uniform magnetic field. The integers represent the LL indices n. This figure is adapted from [9].

From the integration of the equation of motions (1.2), one can finds,

$$\begin{aligned} \dot{x} &= \frac{\Pi_x}{m} = -\omega_B(y - Y), \\ \dot{y} &= \frac{\Pi_y}{m} = \omega_B(x - X), \end{aligned} \tag{2.24}$$

where X, Y are the integration constants. Usage of the above two equations leads us to the definition of the guiding center operators, such that,

$$X = -\frac{\tilde{\Pi}_y}{eB}, \quad Y = \frac{\tilde{\Pi}_x}{eB}. \tag{2.25}$$

From the fact that $[\tilde{\Pi}_x, \tilde{\Pi}_y] = i\hbar^2/l_B^2$ the commutation relation is non-zero:

$$[X, Y] = il_B^2, \tag{2.26}$$

which means that the uncertainty rises as follows,

$$\Delta X \Delta Y = 2\pi l_B^2. \tag{2.27}$$

As a conclusion, the guiding center position is uncertain [2]. The number of the possible quantum states in the uncertain region (the number of the degeneracy) is given by,

$$N_B = \frac{A}{\Delta X \Delta Y} = \frac{A}{2\pi l_B^2} = \frac{BA}{h/e} = \frac{\Phi}{\Phi_0}, \tag{2.28}$$

where A is the area of the uncertain region and Φ_0 is a magnetic flux quantum, and Φ is the magnetic flux of the uncertain region of the guiding center. The term Φ/Φ_0 is called the number of magnetic flux quanta.

2.6 The Role of Uniform Electric Field

In the previous section, we saw that the LLs are massively degenerate and that numerous quantum states share the same energy. Now, we will investigate how this degeneracy is affected and how the LLs change when an external electric field is added to the system.

We consider an electric field $\boldsymbol{E}$ as an extra effect to the uniform magnetic field $\boldsymbol{B}$ in the x-direction. Since we study in the Landau gauge, from the Hamiltonian (2.13), one reads,

$$H = \frac{1}{2m}p_x^2 + \frac{1}{2m}\left(p_y + eBx\right)^2 + eEx, \tag{2.29}$$

where $E = -\frac{\partial\phi}{\partial x}$. We use the same ansatz $\psi_k(x,y) = e^{iky}f_k(x)$ to solve the Schrödinger equation $H\psi_k(x,y) = E_n\psi_k(x,y)$, where E_n are LLs (2.17). One notices that the Scrödinger equation will be similar to Equation (2.21), as follows,

$$H_k f_k(x) = E_n f_k(x), \quad \text{where } H_k = \frac{1}{2m}p_x^2 + \frac{1}{2}m\omega_B^2\left(x + x_k\right)^2 + eEx, \tag{2.30}$$

where I used $x_k \equiv kl_B^2$. The Hamiltonian H_k can be modified as,

$$H_k = \frac{1}{2m}p_x^2 + \frac{1}{2}m\omega_B^2(x^2 + 2xx_c) + \frac{1}{2}m\omega_B^2x_k^2, \tag{2.31}$$

where we define $x_c \equiv x_k + \frac{eE}{m\omega_B^2}$. The above equation can be written in the complete square form by adding and subtracting the $\frac{1}{2}m\omega_B^2x_c^2$. So we have,

$$H_k = \frac{1}{2m}p_x^2 + \frac{1}{2}m\omega_B^2(x + x_c)^2 + \frac{1}{2}m\omega_B^2(x^2 - x_c^2). \tag{2.32}$$

In the above expression, we can use the definition of x_c to simplify the Hamiltonian. The final form of the Hamiltonian can be obtained as,

$$H_k = \frac{1}{2m}p_x^2 + \frac{1}{2}m\omega_B^2(x + x_c)^2 - \frac{m}{2}\left(\frac{E}{B}\right)^2 - eEx_k. \tag{2.33}$$

It is easy to see that the energy depends on both n and k integers, now. It can take the following form [4, 9],

$$E_{n,k} = \hbar\omega_B\left(n + \frac{1}{2}\right) - \frac{m}{2}\left(\frac{E}{B}\right)^2 - eEx_k. \tag{2.34}$$

The first term on the right-hand side represents the degenerate Ladau levels. The extra two terms come from the existence of the electric field $\boldsymbol{E}$. The role of the

uniform electric field lifts massive degeneracy by linear dependency of the k integer. As $\boldsymbol{E} = 0$, we will end up with LLs, meaning that energy levels become massively degenerate in the Equation (2.34).

2.7 Quantization in the Symmetric Gauge

In this section, we solve the Scrödinger equation in the symmetric gauge, which is defined as follows,

$$\boldsymbol{A} = \frac{B}{2}(x\hat{y} - y\hat{x}), \tag{2.35}$$

which allows us to use the advantage of the rotational symmetry. In this gauge, the Hamiltonian (2.14) can be written as,

$$H = \frac{\boldsymbol{p}^2}{2M} + \frac{1}{2}M\bar{\omega}^2\boldsymbol{r}^2 + \frac{1}{2}\omega_B L_z, \tag{2.36}$$

where M is the mass, $\boldsymbol{r} = (x, y, 0)$ is the position vector, and $\bar{\omega} = \omega_B/2$ is the effective cyclotron frequency.

We use the operator method, since it is hard to solve the Schrödinger equation for the Hamiltonian in the symmetric gauge (2.36). If the annihilation operator (2.15) acts on the ground state wave function $|n = 0\rangle$, the result will vanish $a\,|n = 0\rangle = 0$. We can solve the ground state wave function by using this relation. From the Equation (2.15), the creation and annihilation operators can be calculated as,

$$a = -i\sqrt{2}\left(l_B\bar{\partial} + \frac{z}{4l_B}\right), \quad a^\dagger = i\sqrt{2}\left(l_B\partial - \frac{\bar{z}}{4l_B}\right), \tag{2.37}$$

where $z \equiv x - iy$, and $\bar{z} \equiv x + iy$ and also holomorphic and anti-holomorphic derivatives are defined as,

$$\partial \equiv \frac{1}{2}\left(\frac{\partial}{\partial_x} + i\frac{\partial}{\partial_y}\right), \quad \bar{\partial} \equiv \frac{1}{2}\left(\frac{\partial}{\partial_x} - i\frac{\partial}{\partial_y}\right). \tag{2.38}$$

To solve the ground state wave function from the equation $a\,|0\rangle = 0$, we use the chain rule to change the variables of the derivatives from x, y to complex coordinates z. Assume $\psi_0 = \psi_0(z, \bar{z})$, where $\psi_0 = |0\rangle$ is the ground state. From the chain rule, one can find

$$\frac{\partial}{\partial x} = \frac{\partial}{\partial z} + \frac{\partial}{\partial \bar{z}}, \quad \frac{\partial}{\partial y} = -i\frac{\partial}{\partial z} + i\frac{\partial}{\partial \bar{z}}. \tag{2.39}$$

As a result, the holomorphic derivatives (2.38) will be $\partial = \partial/\partial\bar{z}$. Similarly, the anti-holomorphic one equals $\bar{\partial} = \partial/\partial z$. So, the equation $a\psi_0 = 0$ transforms to a partial differential equation. We have,

$$\frac{\partial\psi_0}{\partial\bar{z}} = -\frac{z}{4l_B^2}\psi_0. \tag{2.40}$$

The solution of the partial differential equation is given by,

$$\psi_0(z,\bar{z}) = f(z)e^{-|z|^2/4l_B^2}, \tag{2.41}$$

for any holomorphic function $f(z)$. The above wave function does not imply the degeneracy in the ground state $n = 0$. The uncertainty of guiding centers can be used to implement the degeneracy. The Hamiltonian (2.14) commutes with the guiding center operators (2.25), resulting in $[H, \tilde{\Pi}_\mu] = 0$ where $\mu = \{x, y\}$. Since pseudo-momentum commutes with the Hamiltonian in the symmetric gauge, the pseudo-momentum does not change with time, according to the Heisenberg equation of motion $\dot{\tilde{\Pi}}_\mu = 0$. So, the pseudo-momentum does not contribute to the energy, and it only refers to the degeneracy in the ground state. We can define new operators in terms of pseudo-momentum $\tilde{\Pi}_\mu$ that refer to degeneracy in the LLL [9]:

$$b = \frac{1}{\sqrt{2e\hbar B}}\left(\tilde{\Pi}_x - \tilde{\Pi}_y\right), \quad b^\dagger = \frac{1}{\sqrt{2e\hbar B}}\left(\tilde{\Pi}_x + \tilde{\Pi}_y\right), \tag{2.42}$$

where $[b, b^\dagger] = 1$. Now, the new good quantum number m can be introduced to label degenerate states in the LLL. So, the Hilbert space is spanned by $|n\rangle \otimes |m\rangle = |n, m\rangle$, that satisfy the following equation,

$$|n, m\rangle = \frac{(a^\dagger)^n (b^\dagger)^m}{\sqrt{n!m!}} |0, 0\rangle . \tag{2.43}$$

The other degenerate ground state is calculated by acting the $b^\dagger$ operator on the LLL wave function $\psi_{0,m}$, where $n = 0$. For the $m = 1$ we have,

$$b^\dagger\psi_{n=0,m=1} = -\frac{i}{\sqrt{2}}\frac{z}{l_B}e^{-|z|^2/4l_B^2}. \tag{2.44}$$

The above result can be generalized as,

$$\psi_m \propto \left(\frac{z}{l_b}\right)^m e^{-|z|^2/4l_B^2}, \tag{2.45}$$

where we can ignore the $n = 0$ index and the $-i/\sqrt{2}$ coefficient since we'll normalize the wave function. The above single-particle wave functions are also an exact solution

for the angular momentum operator in the z-direction, such that,

$$L_z\psi_m = \hbar m\psi_m, \tag{2.46}$$

where m is the positive angular momentum quantum number. Finally, the normalized single-particle degenerate ground state wave functions can be calculated as [4, 9, 14],

$$\psi_m(z,\bar{z}) = \frac{1}{\sqrt{2\pi 2^m m! l_B}} \left(\frac{z}{l_b}\right)^m e^{-|z|^2/4l_B^2}. \tag{2.47}$$

2.8 Treatment of Conductivity

First, we'll understand the connection between Hall resistivity ρ_H and experimental result of the integer quantum Hall effect (2.1). Start with the Hall resistivity, which is derived from the Drude model (1.17):

$$\rho_H = \frac{B}{ne}, \tag{2.48}$$

which can be modified as follows,

$$\rho_H = \frac{h}{e^2}\frac{BA}{h/e}\frac{1}{nA}, \tag{2.49}$$

where A is the area of the sample. We can use the fundamental quantities such as magnetic flux $\Phi = BA$ enclosed by area A, the total number of electrons $N = nA$, and flux quantum $\Phi_0 = h/e$, to rewrite the above equation [4]:

$$\rho_H = \frac{h}{e^2}\frac{\Phi}{\Phi_0}\frac{1}{N} = \frac{h}{e^2}\frac{N_\Phi}{N}, \tag{2.50}$$

where $N_\Phi \equiv \Phi/\Phi_0$ is the number of flux quanta. We can compare this quantity with the experimental observation (2.1), allowing us to identify the filling fraction ν in terms of fundamental definitions:

$$\nu \equiv \frac{N}{N_\Phi}. \tag{2.51}$$

A more realistic picture can be depicted by using the current operator $\hat{I}$ in quantum mechanics [9]. The current operator equals the expected value of the mechanical momentum operator $\mathbf{\Pi} = \boldsymbol{p} + e\boldsymbol{A}$ such that,

$$\hat{I} = -\frac{e}{m}\sum_{n=1}^{\nu}\sum_{k}\langle\psi_{n,k}|\mathbf{\Pi}|\psi_{n,k}\rangle\,, \tag{2.52}$$

where $\psi_{n,k}$ is LL wave functions in the Landau gauge (2.22), and $1 \leq n \leq \nu$ represents the filled LLs. From the definition of the mechanical momentum operator, the components of the current operator $I_\mu = -e\dot{\mu} = -\frac{e}{m}\Pi_\mu$, in the Landau gauge, can be found as

$$I_x = -\frac{e}{m}\langle p_x \rangle , \quad I_y = -\frac{e}{m}\langle p_y + exB \rangle . \tag{2.53}$$

We will calculate the current operator in the presence of uniform magnetic and electric fields. The wave functions are $\psi_{n,k} = e^{iky}\psi_{\text{SHO}}(x+x_c)$, where $\psi_{\text{SHO}}(x+x_c)$ is shifted wave functions of the simple harmonic oscillator by $x_c = kl_B^2 + \frac{mE}{eB^2}$, that governs to the Hamiltonian (2.33). The x-component of the current operator vanishes, since the expectation value of the momentum operator in the basis of the simple harmonic oscillator is zero:

$$I_x = -\frac{e}{m}e^{2iky}\sum_{n=1}^{\nu}\sum_{k}\langle \psi_{\text{SHO}}|p_x|\psi_{\text{SHO}}\rangle = 0, \tag{2.54}$$

Similarly, the y-component of the current operator can be calculated as,

$$I_y \propto \hbar k + eB\langle x \rangle , \tag{2.55}$$

where we used $\langle p_y \rangle = -i\hbar\langle \psi_{n,k}|\frac{\partial}{\partial_y}|\psi_{n,k}\rangle = \hbar k$. The expectation value of position is equal to the shift amount, which is $\langle x \rangle = x_c$. We have,

$$I_y = -e\sum_{n=1}^{\nu}\sum_{k}\frac{E}{B} = -e\nu N\frac{E}{B}, \tag{2.56}$$

where the summation over k indices equals the number of electrons in the system N. Also current density in the y-direction can be found,

$$J_y = -e\nu N\frac{E}{BA}. \tag{2.57}$$

We found that the x-component of the current operator vanishes, $I_x = 0$, as a result, $J_x = 0$. Also note that, since $\boldsymbol{I} \perp \boldsymbol{E}$, the only x-component of the electric field is not zero $E_x \neq 0$. From the conductivity tensor (1.12), one reads $J_y = \sigma_{xy}E$. We have,

$$\sigma_{xy} = \frac{Ne\nu}{BA}, \tag{2.58}$$

where we used the Equation (2.57). In the context of IQHE, the LLs are fully filled (ν is an integer), which means that the number of states must equal the number of electrons in the system. On the other hand, states in the LLs are fully filled. So, we

have $N = N_B = \Phi/\Phi_0$ where N_B is the number of the degeneracy (2.28). We can use this case to get,

$$\sigma_{xy} = \frac{e^2}{h}\nu, \tag{2.59}$$

or equivenlty, $\rho_H = \frac{h}{e^2}\frac{1}{\nu}$. This is the exact experimental result of the IQHE (2.1).

2.8.1 $\boldsymbol{E} \times \boldsymbol{B}$ Drift

The drift velocity is crucial for understanding the edge states that we cover in the next chapter. Consider a uniform magnetic field in the z-direction $\boldsymbol{B} = B\hat{z}$ and a zero electric field $\boldsymbol{E} = 0$ in the stationary laboratory frame. Let there be a moving frame of reference that has $v_f = -v\hat{x}$ velocity relative to the laboratory reference frame. In the moving frame of reference, the velocity of the laboratory, called the drift velocity, is $v_d = -v_f = v\hat{x}$. The Electric and magnetic fields transform by the Lorentz transformation as follows,

$$\begin{aligned} &\boldsymbol{B}'_{\parallel} = \boldsymbol{B}_{\parallel}, \quad \boldsymbol{E}'_{\parallel} = \boldsymbol{E}_{\parallel}, \\ &\boldsymbol{B}'_{\perp} = \gamma\left(\boldsymbol{B}_{\perp} - \frac{1}{c^2}\boldsymbol{v}\times\boldsymbol{E}\right), \quad \boldsymbol{E}'_{\perp} = \gamma(\boldsymbol{E}_{\perp} + \boldsymbol{v}\times\boldsymbol{B}), \end{aligned} \tag{2.60}$$

where $\gamma = 1/\sqrt{1-(v/c)^2}$ is called the Lorentz factor, and the prime indices represent the vector fields in the moving frame of reference. While the parallel sub-indices show the $x-y$ plane component, the perpendicular ones show the z-component. We assume that the magnitude of the velocity is much smaller than the speed of light $v << c$, so the γ factor goes to identity. From the Lorentz transformation (2.60), the magnetic and electric fields in the moving frame of reference can be obtained as,

$$\boldsymbol{E}'_{\perp} = \boldsymbol{v}_f \times \boldsymbol{B}, \quad \boldsymbol{B}'_{\perp} = \boldsymbol{B}_{\perp}. \tag{2.61}$$

The electric field $\boldsymbol{E}'$ is generated by the relative motion in the moving frame, even though the electric field is zero in the laboratory frame of reference. The velocity of the moving frame of reference relative to the laboratory frame v_f can be obtained as,

$$\boldsymbol{v}_f = \frac{\boldsymbol{E}'_{\perp}\times\boldsymbol{B}}{B^2}. \tag{2.62}$$

which is called the *drift* velocity $\boldsymbol{v}_d$. Notice that the drift velocity $\boldsymbol{v}_d$ is perpendicular to both $\boldsymbol{E}'$ and $\mathbf{B}$ and is independent of the electron's charge and mass, making it universal for all electrons in the system.

The drift velocity $\boldsymbol{v}_d$ provides the microscopic mechanism for the quantized Hall resistivity ρ_H by ensuring that all electrons move with the same velocity. The drift current density can be calculated by $\boldsymbol{J}_d = -ne\boldsymbol{v}_d$, resulting in,

$$\boldsymbol{J}_d = -ne\frac{\boldsymbol{E}'_\perp \times \boldsymbol{B}}{B^2}. \tag{2.63}$$

We have the current density in the x-direction, such that,

$$J_x = -ne\frac{E_y}{B}, \tag{2.64}$$

From the conductivity tensor (1.12), one reads,

$$\begin{aligned} J_x &= \sigma_{xx}E_x + \sigma_{xy}E_y, \\ J_y &= \sigma_{xy}E_x + \sigma_{yy}E_y. \end{aligned} \tag{2.65}$$

From the equation (2.64), the components $J_y = E_x = 0$. We have,

$$\sigma_{yy} = 0, \sigma_{xy} = \frac{J_x}{E_y} = -\frac{ne}{B}. \tag{2.66}$$

As $\sigma_{yy} = 0$, the σ_{xx} also must vanish. Consequently, the conductivity tensor (inverse of the resistivity tensor $\boldsymbol{\sigma}$) is the same result as the Drude model in Equation (1.17).

2.9 Edge States

The edge of the Hall sample is modelled by a confinement potential $V_{\text{conf.}}(x)$. We consider a Hall sample which has a finite size in the x-direction. Note that the confinement potential breaks the translation symmetry in the x-direction. Under the uniform magnetic field, the Hamiltonian (2.21) becomes, The Hamiltonian:

$$H = \frac{p_x^2}{2m} + \frac{1}{2}m\omega_B^2(x + x_k)^2 + V_{\text{conf}}(x). \tag{2.67}$$

Remember that the wave functions are localised simple harmonic oscillator around $x_k = kl_B^2$. Also, we assume that the confinement potential changes smoothly as a function of x. Therefore, we can Taylor expand the confinement potential around the localised position $x_k = kl_B^2$. We have,

$$V_{\text{conf}}(x) \approx V_{\text{conf}}(x_k) + (x - x_k)\frac{\partial V_{\text{conf}}}{\partial x}\Big|_{x_k} + \mathcal{O}\left(\frac{\partial^2 V_{\text{conf.}}}{\partial y^2}\right). \tag{2.68}$$

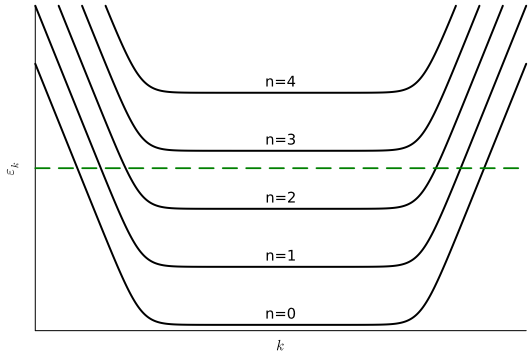

Figure 2.3: The dispersion relation of the confinement model. The Fermi level, represented by a horizontal green-dashed line. The band of the bulk is degenerate LLs, which are labeled by n, but due to the effect of the confinement potential, the degeneracy is lifted smoothly on the edges, resulting in bending energy levels. This figure is adapted from [4]

The quadratic terms can be neglected in the expansion. The Hamiltonian (2.67) will be,

$$H = \frac{p_x^2}{2m} + \frac{1}{2}m\omega_B^2(x + x_k)^2 + (x - x_k)eE_{\text{conf}} + V_{\text{conf}}(x_k), \tag{2.69}$$

where E is the electric field that is generated by the confinement potential $V_{\text{conf}}(x)$. The above Hamiltonian is equivalent to the following Hamiltonian,

$$H = \frac{p_x^2}{2m} + \frac{1}{2}m\omega_B^2(x + x_c)^2 + V_{\text{conf}}(x_c) - \frac{1}{2}mv_d^2, \tag{2.70}$$

where $v_d = E/B$ is the drift velocity. The wave functions are localised at the position $x_c = x_k + \frac{eE}{m\omega_B^2}$ in where the simple harmonic wave functions are shifted by x_c in the presence of an electric field. So, we have the same Hamiltonian that describes LLs in the presence of an electric field (2.33). The eigenvalues (2.34) consist of the LLs (cyclotron motions) plus local potential energy, resulting in bending energy levels (Figure 2.3).

Getting the same Hamiltonian is not surprising, because the eigenvalues of the model are solved (2.34), and the group velocity of the states, $\psi_{n,k} = e^{iky}\psi_{\text{SHO}}(x + x_c)$ is given by,

$$v_g = \frac{1}{\hbar}\frac{\partial \epsilon_{n,k}}{\partial k} = \frac{E}{B}, \tag{2.71}$$

which is equal to the drift velocity v_d. The drift velocity can be expressed in terms of

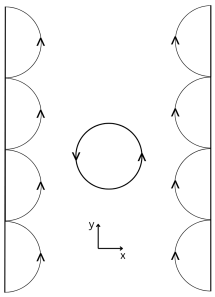

Figure 2.4: Cylotron orbits under the uniform magnetic field. The full cyclotron motion corresponds to the states that are described by the LL energies in the bulk. The half-cyclotron orbits represent the edge motion that moves along the x-direction due to the non-zero drift velocity. This figure is adapted from [16].

confinement potentials as follows,

$$v_g = \frac{E}{B} = \frac{1}{eB}\frac{\partial V_{\text{conf}}}{\partial x}. \tag{2.72}$$

The electrons move along in specific directions that depend on the sign of the group velocity v_g. The semi-classical interpretation is that while electrons have motion in the bulk with the cyclotron frequency ω_B, they have skipping orbits (half-cyclotron motion) along the edge of the sample with non-zero group velocity v_d (Figure 2.4).

The edge states can carry the current by introducing a potential difference $\Delta\mu$ between the two sides of the sample[2, 4, 9, 10]. The current in the x-direction can be calculated as,

$$I_y = -e\int \frac{dk}{2\pi} v_g = \frac{1}{2\pi}\frac{1}{B}\int dk \frac{\partial V_{\text{conf}}}{\partial x}\Big|_{x_k}. \tag{2.73}$$

Since $x_k = kl_B^2$, we can change the measurement of the integral from k variable to x_k variable. We have,

$$I_y = \frac{1}{2\pi}\frac{1}{Bl_B^2}\int dx_k \frac{\partial V_{\text{conf}}}{\partial x}\Big|_{x_k} = \frac{e}{2\pi\hbar}\Delta\mu. \tag{2.74}$$

where we used $V_H = V_{\text{conf}}$. From the definition of off-diagonal conductance tensor elements, one reads,

$$\sigma_{xy} = \frac{I_y}{V_H} = \frac{e^2}{h} \tag{2.75}$$

where V_H is the Hall voltage, and we used $\Delta\mu = eV_H$. For n filled LLs:

$$\sigma_{xy} = \frac{e^2}{h}\nu \tag{2.76}$$

where $\nu = n$ for fully filled LLs. This result is the expected conductivity for n LLs.

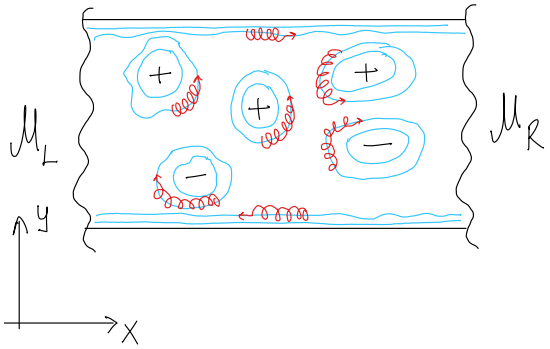

Figure 2.5: A schematic representation of the electrostatic potential landscape due to the random impurities. The current flows through the sample due to the potential difference $\Delta\mu = \mu_R - \mu_L$. The blue lines indicate the equipotential regions that are created by the positive and negative impurities. The red arrows indicate the cyclotron motion, which is constrained by the equipotential lines. The equipotential lines become straight near the edge due to the confinement potential in the x-direction. This figure is adapted from [2].

2.10 Disorder & Percolation

The IQHE experiments come with the disorder that already exists on the Hall bar, and interestingly, the quantization of the Hall resistivity ρ_H is the direct consequence of the disorder. This disorder breaks the symmetries of the system, as we've seen in the previous chapter. We have already covered the value of the quantization, which is $\rho_H = \frac{h}{e^2}\frac{1}{\nu}$, but haven't yet seen why the quantum Hall plateaux occur at integer filling fractions ν.

The potential landscape picture (Fig. 2.5) provides a useful connection between filled LLs and the quantization of the conductivity σ_{xy}. We consider a random impurity potential landscape V_{imp} with the existence of a confinement potential V_{conf} on the Hall sample. Random impurity charges ($\pm$ symbols in the Figure 2.5) confine the electrons as a localised state in the bulk of the sample.

The impurity potentials reveal equipotential lines on the Hall bar, and the electrons' cyclotron motion lies on the equipotential lines (Figure 2.5). The cyclotron orbit

moves in the direction of clock-wise for positively charged impurities with the drift velocity v_d and vice versa for negatively charged ones. To see this, we write the Heisenberg equation of motion of the guiding center operators (2.25) as follows,

$$i\hbar\dot{X} = [H, X] = [H_0, X] + [V_{\text{imp}}(X, Y), X]. \tag{2.77}$$

where $H_0 = \frac{\boldsymbol{\Pi}^2}{2m}$. Since, in the symmetric gauge $[\Pi_i, \tilde{\Pi}_j] = 0$, the commutation relation vanishes $[H_0, X] = 0$. We have,

$$i\hbar\dot{X} = -\frac{\partial V_{\text{imp}}}{\partial X}[X, Y] = -il_B^2\frac{\partial V_{\text{imp}}}{\partial X}, \tag{2.78}$$

where we used the fact that $[A, F(A, B)] = \frac{\partial F}{\partial B}[A, B]$ where $[A, B] \neq 0$. Also, we used the commutation relation between guiding center operators $[X, Y] = il_B^2$. The equation of motion for the x-component of the guiding center operator will be,

$$\dot{X} = \frac{E_y}{B} \tag{2.79}$$

in the local electric field $e\boldsymbol{E} = -\frac{\partial V_{\text{imp}}}{\partial X}$. Similarly,

$$\dot{Y} = -\frac{E_x}{B}. \tag{2.80}$$

We notice that $\dot{\boldsymbol{R}} \perp \Delta V_{\text{imp}}$. Therefore, the guiding center moves on the equipotential lines with the drift velocity v_d.

The density of states $D(\mathcal{E})$ is useful to create a connection between disorder and quantization. In the presence of a uniform magnetic field $\boldsymbol{B}$ and the impurities on the sample, the density of states takes the form of a Gaussian shape (C case in the Figure 2.6). If electrons occupied the localised state in the DOS, we have an insulator; otherwise, we have a conductor where the electrons occupied the extended states.

Imagine that we start with the zero DOS at the beginning (first column in the Figure 2.7), where the Fermi energy ϵ_F lies between the LLs gap. In this case, the Hall sample behaves like an insulator. Now, consider that the electron density is controlled by the potential difference $\Delta\mu$. As the potential difference increases (magnetic field $\boldsymbol{B}$ decreases), the electrons start to occupy the dips of the impurity potentials (second column in the Figure 2.7) where electrons occupied the localised states in the DOS. For these two cases, the Hall resistivity ρ_H remains constant (blue dot in the Figure 2.7) because the localised states do not affect the current in the y-direction, and also

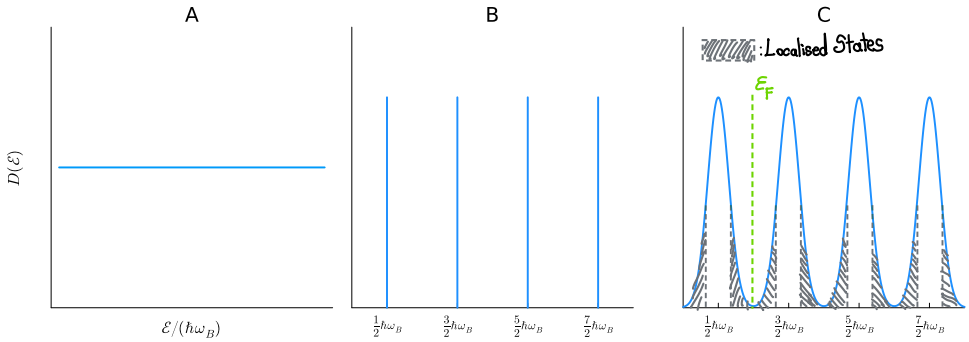

Figure 2.6: Density of states $D(\mathcal{E})$ for a 2D electron gas as a function of energies $\mathcal{E}$. (A) If there is no magnetic field in the system, we have a constant density of states. (B) If there is a magnetic field in the ideal (pure) system, the density of states shows peaks at LLs. (C) If there is a magnetic field in the system that has an impurity, we see broadened density of states where localised(gray shaded areas) and extended states (white areas) occur. This figure is adapted from [9].

the longitudinal resistivity ρ_{xx} is zero (red dot in the Figure 2.7). The current in the system is carried by the edge states. This is exactly what happened in the Hall plateaux (Figure 2.1).

When we reach the threshold percolation, the electron density starts to percolate between the two edges of the Hall sample (last column in the Fig. 2.7), resulting in back-scattering (purple arrows on the bulk in the Figure 2.7) that contributes to the current I_y. At this stage, the Fermi energy ϵ_F is crossing the next LL where the extended states are occupied by the electrons. As the Hall resistivity is decreasing, the longitudinal resistivity shows a peak at the same time, meaning that the Hall bar behaves like a conductor since we have a non-zero I_y.

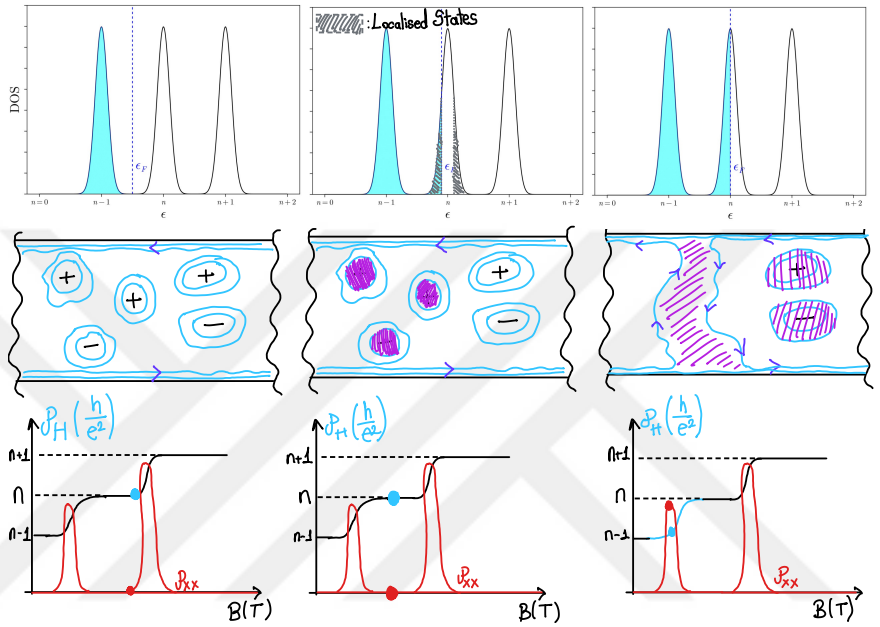

Figure 2.7: Representation of the percolation on the Hall bar. The first row shows the impurity broadened density of states, where the blue dashed line represents the Fermi energy ϵ_F, and LLs are labeled by n. The second row shows the percolation steps on the Hall bar, where the purple area indicates the electron density at potential difference $\Delta\mu$. The last row shows the Hall plateaux, where ρ_H and ρ_{xx} are the Hall and longitudinal resistivities, respectively. This figure is adapted from [2].

CHAPTER 3

FRACTIONAL QUANTUM HALL EFFECT

3.1 Introduction

The Fractional Quantum Hall Effect (FQHE) refers to existing states that are unoccupied in the Landau Levels (LL), which means that electrons partially fill the LLs and the filling fraction ν is not an integer. The electrons need an extra $E_{n+1} - E_n = \hbar\omega_B$ energy cost to occupy the next LL, where $\omega_B = eB/m$ is the cyclotron frequency. The experimental evidence [17, 18] shows that in the partially filled LLs such as $\nu = 1/3, 1/5, 2/7$, etc., the Hall plateau appears and the Hall resistivity is quantized by h/e^2 as follows,

$$\rho_H = \frac{h}{e^2}\frac{1}{\nu}, \tag{3.1}$$

where ν is a non-integer fraction. In the IQHE, the states are fully filled (ν is an integer), which is why, due to the Pauli principle, the electrons are pushed to the next LL to occupy empty states. But, in the FQHE picture, the situation is different. Electrons in the same LL share a fixed kinetic energy and cannot occupy higher LLs despite the presence of unfilled states [2]. Therefore, the massive degenerate LLs appear.

The total number of states on each LL equals the number of flux quanta $N_\Phi = \Phi/\Phi_0$, where Φ is the magnetic flux enclosed by the sample area A and Φ_0 is the flux quantum. The number of ways to occupy empty states at the filling factor ν is given by,

$$\binom{N_\Phi}{\nu N_\Phi}, \quad \nu N_\Phi \in \mathbb{Z}^+ \tag{3.2}$$

which is only valid for fermions, since they can't occupy the same state. As an example, we have two empty states and one of them is occupied by one electron ($\nu = 1/2$),

and let the number of states be $N_\Phi = 2$. In this case, the number of ways to occupy these states equals $\binom{2}{1} = 2$, as expected. So, we have two degenerate states on each LLs. But the problem contains huge complexity for a larger number of available states N_Φ. You can see the number of degeneracies on each LL as a function of the number of available states N_Φ in the Figure (3.1). We immediately notice that the degeneracy (number of orbitals in a LL) grows linearly with N_Φ, making computational and numerical calculations increasingly important.

The interaction among particles matters, since the kinetic energy is the same for all electrons on the same LL. The main role of the interaction is to lift the massive degeneracy on LLs (3.2), resulting in one linear combination of degenerate states becoming a unique and non-degenerate ground state (LLL). We will see that the interaction Hamiltonian has a unique ground state thanks to the interactions among particles.

3.2 Two-Body Problem

The most basic many-body problem is the two-body problem whose Hamiltonian can be written as,

$$H = \frac{1}{2m_1}\mathbf{\Pi}_1^2 + \frac{1}{2m_2}\mathbf{\Pi}_2^2 + V_{\text{int}}, \tag{3.3}$$

where V_{int} is the interaction potential between two particles (i.e., Coulomb interaction) and $\mathbf{\Pi}$ is mechanical momentum in the presence of a magnetic field. The kinetic part can be decomposed into two decoupled relative and center-of-mass equations. Mechanical momentum $\mathbf{\Pi} = \boldsymbol{p} + e\boldsymbol{A}(\boldsymbol{r})$ in the uniform magnetic fields, namely [4],

$$\begin{aligned} \mathbf{\Pi}_{\text{CM}} &= \mathbf{\Pi}_1 + \mathbf{\Pi}_2 \\ \mathbf{\Pi}_{\text{rel}} &= \frac{\mathbf{\Pi}_1 - \mathbf{\Pi}_2}{2}. \end{aligned} \tag{3.4}$$

where (rel, CM) sub-indices represent the relative and center-of-mass, respectively. The part of the kinetic energy for two particles becomes,

$$T = \frac{1}{2m}\left(\mathbf{\Pi}_1^2 + \mathbf{\Pi}_2^2\right) = \frac{1}{4m}{\mathbf{\Pi}_{\text{CM}}}^2 + \frac{1}{2m}{\mathbf{\Pi}_{\text{rel}}}^2, \tag{3.5}$$

where we choose equal masses $m = m_1 = m_2$. The kinetic energy T describes the electrons' movement under the uniform magnetic field. The interaction between

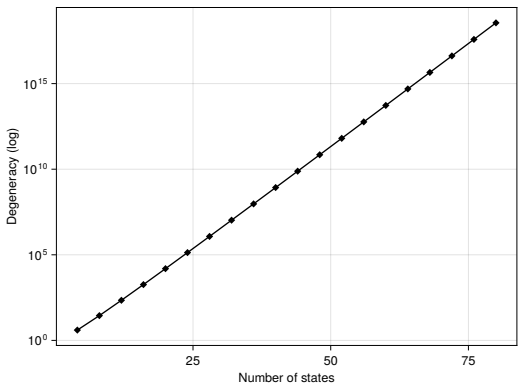

Figure 3.1: The number of degeneracies on each LLs (Equation 3.2) making problem hard to solve analytically.

particles only depends on the relative coordinates, such that,

$$V_{\text{int}} = V(|\boldsymbol{r}_1 - \boldsymbol{r}_2|). \tag{3.6}$$

The center of mass and the relative part of the Hamiltonian (3.3) become,

$$H_{\text{CM}} = \frac{1}{4m}\boldsymbol{\Pi}_{\text{CM}}{}^2, \quad H_{\text{rel}} = \frac{1}{2m}\boldsymbol{\Pi}_{\text{rel}}{}^2 + V(|\boldsymbol{r}_1 - \boldsymbol{r}_2|). \tag{3.7}$$

We have already solved the Schrödinger equation for the center-of-mass part in the IQHE section, where eigenvalues are LLs (2.17) and wave functions are given by (2.22 and 2.47). But the relative part is hard to solve due to the existence of the interaction term. That is why we use the approximation called the lowest Landau level (LLL). In this scenario, the kinetic energy becomes a fixed constant, and the wavefunctions adopt a uniquely simple mathematical form, making the complex many-body problem much easier to solve.

For the one-particle case, the ground state (LL) wave function is given uniquely by the Equation (2.41). Now we can use this wave function $\Psi_0(z) = f(z)e^{-|z|^2/4l_B^2}$ to solve the two-body problem (3.7), where zero indices represent LL and $f(z)$ is an analytical function. The two-body wave function in the LLL can be written as [4, 9],

$$\Psi_{m,M}(z_1, z_2) \propto (z_1 - z_2)^m (z_1 + z_2)^M e^{-(|z_1|^2+|z_2|^2)/4l_B^2}, \tag{3.8}$$

where m and M are non-negative integers that represent the relative and center-of-mass angular momentum, respectively. We also ignore the normalization term. Note

that the relative angular momentum m must be even for bosons and odd for fermions, providing exchange symmetry between particles. This wave function is the exact and unique ground state for any interaction terms $V(|\boldsymbol{r}_1 - \boldsymbol{r}_2|)$ in the two-particle LLL sub-space, since we are sure that the LLL wave function is given by $\Psi_0(z) = f(z)e^{-|z|^2/4l_B^2}$. As a result, we write the wave function of the two-body problem without solving the Schrödinger equation with a complicated potential term $V(|\boldsymbol{r}_1 - \boldsymbol{r}_2|)$. This is the power of LLL approximation.

3.3 Many-Body Problem

The Hamiltonian for many-body particles is given by [10, 14],

$$H = \sum_{i=1}^{N} \frac{1}{2m_i} \boldsymbol{\Pi}_i^2 + \sum_{i<j} V_{\text{int}}(\boldsymbol{r}_i - \boldsymbol{r}_j), \tag{3.9}$$

where N is the total number of particles. It is hard to solve the Schrödinger equation for this problem in the LLL. We cannot generalize the two-body wave function (3.8) to find a solution of the many-body Hamiltonian (3.9). Again, the unique LLL wave function for N particles must satisfy the following form [9],

$$\Psi(z_1, z_2, \ldots, z_N) = f(z_1, z_2, \ldots, z_N) e^{-\sum_{i=1}^{N} |z_i|^2/4l_B^2}. \tag{3.10}$$

However, it is hard to explain fermionic or bosonic behavior at any filling fraction ν to explain FQHE by using the above form.

The more robust way to construct the analytical function $f(z_1, z_2, \ldots, z_N)$ is the Slater determinant, which automatically anti-symmetrizes the wave function for fermions. For the N particle system, the Slater determinant is:

$$f(z_1, z_2, \ldots, z_N) = \begin{vmatrix} z_1^0 & z_2^0 & \cdots & z_N^0 \\ \vdots & \vdots & \ddots & \vdots \\ z_1^N & z_2^N & \cdots & z_N^N \end{vmatrix} = \prod_{i<j}^{N} (z_i - z_j), \tag{3.11}$$

where we ignore the minus sign since it is not important here. This form is called the Vandermonde polynomial, whose exponent is odd, making the $f(z_1, z_2, \ldots, z_N)$ anti-symmetric under the exchange between particles. Let there be N available states on the LLL. The term with the highest exponent in the Vandermonde polynomial

is z^{N-1}. Therefore, the highest possible single particle angular momentum $m_{\text{max}} = N-1$ is occupied by one electron. As we mentioned, the function $f(z_1, z_2, \ldots, z_N)$ is fermionic (anti-symmetric), due to the Pauli principle, there are no electrons occupy the same angular momentum state m. As a result, all N states from $m = 0$ to $m = N - 1$ must be occupied, meaning that we study at filling fraction $\nu = 1$.

So far, we constructed the many-body LLL wave function at $\nu = 1$, which is given by [4],

$$\Psi(z_1, z_2, \ldots, z_N) = \prod_{i<j}^{N} (z_i - z_j) e^{-\sum_{i=1}^{N} |z_i|^2/4l_B^2}, \tag{3.12}$$

which are unique eigenstates in the LLL according to the above discussions. It is important to note that the polynomial term increases as it keeps particles apart, while the exponential part decreases significantly as long as the particles remain separated and away from the origin.

3.4 Laughlin Wave Function

The many-body LLL wave function was introduced by Robert B. Laughlin in 1983 for any filling fraction ν [19]:

$$\Psi_m(z_1, z_2, \ldots, z_N) = \prod_{i<j}^{N} (z_i - z_j)^m e^{-\sum_{i}^{N} |z_i|^2/4l_B^2}, \tag{3.13}$$

where $m = 1/\nu$. Numerical investigations [20] demonstrate that the Laughlin wave function accurately describes the FQHE states in the lowest Landau level. As $m = 1$, the wave function is reduced to the form that describes the ground state for the fully filled LLs (3.12). Historically, the first evidence of the fractional quantum Hall effect (FQHE) appeared at $\nu = 1/3$ [21]. Laughlin's ansatz (3.13) provides an answer for the observation at $\nu = 1/3$ with $m = 3$ for this scenario.

3.4.1 Plasma Analogy

Calculating the expectation values of any operator in the basis of the LLL is challenging for many-body systems. As an example, consider an expectation value of any

operator $\hat{O}(z)$, which is a function of a complex coordinate:

$$\langle \hat{O}(z) \rangle = \frac{\int dz_1^2 dz_2^2 ... dz_N O(z) |\psi_m(z)|^2}{\int dz_1^2 dz_2^2 ... dz_N |\psi_m(z)|^2}, \tag{3.14}$$

where ψ_m is the Laughlin wave functions (3.13). There is no analytic way to evaluate the above integral (3.14), but the many-body wave function can be interpreted beautifully with the useful analogy. The denominator in the expectation value (Equation 3.14) is similar to the partition function, which is given by,

$$Z = \int e^{-\beta U(z_1, z_2, ..., z_N)} dz_1^2 dz_2^2 ... dz_N \tag{3.15}$$

where $\beta = (k_B T)^{-1}$ is the inverse temperature. This analogy leads to a basic relation:

$$e^{-\beta U(z_1, z_2, ..., z_N)} = |\psi_{m,M}|^2. \tag{3.16}$$

We can solve the U function from the above equation. First we set $\beta = 1/m$, we have [22],

$$U(z_1, z_2, \ldots, z_N) = -2m^2 \sum_{i<j}^{N} \ln |z_i - z_j| + \frac{m}{2l_B^2} \sum_{i=1}^{N} |z_i|^2. \tag{3.17}$$

There is a beautiful analogy between plasma physics and the function $U(z_1, z_2, \ldots, z_N)$. Start by considering a differential form of Gauss's Law (in cgs units) in three dimensions:

$$\nabla \cdot \boldsymbol{E} = 4\pi\rho, \tag{3.18}$$

where $\rho = q\delta^{(3)}(\boldsymbol{r})$ is the charge density at the origin, and q is the charge. Evaluate the integral on both sides of the equation, and applying the divergence theorem leads to,

$$\boldsymbol{E} = \frac{q}{r^2}\hat{r}, \quad \phi = \frac{q}{r}\hat{r}. \tag{3.19}$$

To apply the same process to the two dimensions, we use the following analogy,

$$\begin{cases} \text{3D} : A = 4\pi r^2, \text{ and } E \propto r^{-2} \\ \text{2D} : l = 2\pi r, \text{ and } E \propto r^{-1}, \end{cases} \tag{3.20}$$

where A is the area, and d is the length measurements. So, the Gauss law in two dimensions is:

$$\int \boldsymbol{E} \cdot d\boldsymbol{A} = 2\pi q. \tag{3.21}$$

As a result, we have,

$$\boldsymbol{E} = \frac{q}{r}\hat{r}, \quad \phi = -q\ln(r). \tag{3.22}$$

We can compare the $\phi = -q\ln(r)$ term and the $U(z_1, z_2, \ldots, z_N)$ function, which is calculated in the equation (3.17). As a result, immediately, we see that the first term in the $U(z_1, z_2, \ldots, z_N)$ function is the interaction potential energy for the m charged particles. Now consider the following two-dimensional Poisson equation,

$$\nabla^2\left(\frac{|z|^2}{4l_B^2}\right) = \frac{1}{l_B^2} = 2\pi\rho_B, \tag{3.23}$$

where $\rho_B = \frac{1}{2\pi l_B^2}$ is the uniform density. This equation represents the electrostatic potential of a uniform and constant ρ_B density. This result shows that the second term of the Equation (3.17) refers to the interaction of charged m particles with the background potential. As a result, the equation (3.17) is the potential energy of the m charged particles whose density is constant and equals $\rho_B = \frac{1}{2\pi l_B^2}$ [4, 10, 22].

When we slightly decrease the magnetic field B, the number of available quantum states $N_\Phi = BA/\Phi_0$ also decreases. However, the density remains constant, defined as $\rho_B = 1/A_{\text{surface}}$. This change in magnetic field B leads to fewer available states in the filled LLs than there are electrons. It's because the space available for each quantum state $2\pi l_B^2$ has expanded, reducing the total number of states N_Φ that can fit within the fixed surface area A_{surface}. The electrons, however, are still there, so they outnumber the available states. This forces some of the electrons to be promoted to the next available LL. This promotion requires a large, finite amount of energy because of the energy gap between LLs $\Delta E = \hbar\omega_B$. Therefore, an infinitesimally small change in the magnetic field leads to a large energy cost, making the system resistant to changing its density, called incompressible, and it is equivalent to having a bulk excitation gap. In this sense, Laughlin's many-body wave function is called an incompressible quantum liquid, where liquid refers to constant density [2, 9, 19, 22].

3.5 Haldane Pseudopotential

In the previous chapter, we discussed that the kinetic energy is completely quenched, indicating that all states within the LLL are degenerate. Since kinetic energy is fixed,

the interactions dominate the energy scale. That is why we need to determine how electrons interact in the LLL subspace.

Let the eigenvalues of any central interaction potential $V(|\boldsymbol{r_1} - \boldsymbol{r_2}|)$ be $v_{m,M}$, where m is relative angular momentum and M is center-of-mass angular momentum. The eigenvalues can be calculated in the basis of two-body LLL, as [4, 23],

$$v_{m,M} = \frac{\langle m, M|V(|\boldsymbol{r_1} - \boldsymbol{r_2}|)|m, M\rangle}{\langle m, M|m, M\rangle}, \tag{3.24}$$

where $|m, M\rangle$ is the LLL two-body wave function (Equation 3.8), and $\langle m, M|m, M\rangle$ is the normalization term. The $v_{m,M}$ called Haldane pseudo-potential [23]. We can simplify the integral by decomposing coordinates into the center of mass and relative complex coordinates:

$$\begin{aligned} z &= z_1 - z_2 \\ Z &= \frac{1}{2}(z_1 + z_2). \end{aligned} \tag{3.25}$$

The LLL two-body wave function can be written as,

$$|m, M\rangle \propto \phi_{\text{rel}}(z)\phi_{\text{CM}}(Z), \tag{3.26}$$

where $\phi_{\text{rel}}(z) = z^m e^{-|z|^2/8l_B^2}$ is the relative part, and $\phi_{\text{CM}}(Z) = (2Z)^M e^{-|Z|^2/2l_B^2}$. As long as the interaction potential only depends on relative coordinates, the Haldane pseudo-potential (3.24) becomes independent of center-of-mass coordinates, such that,

$$v_m = \frac{\int dz|\phi_{\text{rel}}(z)|^2 V(z)}{\int dz|\phi_{\text{rel}}(z)|^2}. \tag{3.27}$$

Now consider contact interaction $V(\boldsymbol{r}) = g\delta^{(2)}(\boldsymbol{r})$. We study in the 2D geometry, where the coupling constant takes a different form than $g_{3D} = 4\pi\hbar^2 a_s/M$, where a_s is the s-wave scattering length. The 2D coupling constant is approximately given by [24],

$$g_{2D} \approx \frac{\sqrt{8\pi}\hbar^2 a_s}{M a_z}, \tag{3.28}$$

where $a_z = \sqrt{\frac{\hbar}{M\omega_z}}$ is oscillator length in the $z-$ direction and ω_z is the rap frequency in the same direction. So, the integral vanishes unless $m \neq 0$. We have,

$$v_0 = \frac{g_{2D}}{2\pi l_B^2}. \tag{3.29}$$

The density of the LLL wave functions $|\psi_m(z)|^2$, gives useful information about eigenvalues of the model (3.24) for any interaction potential. First we compute the $|\psi_m(z)|^2$, and then we replace $z = re^{im\theta}$. To find the maximum radius of the density, we need to solve r_0 in the following equation,

$$\frac{\partial \psi_m(r_0, \theta)}{\partial r} = 0. \tag{3.30}$$

We will end up with the following maximum radius,

$$r_0 = \sqrt{2m} l_B. \tag{3.31}$$

Correspondingly, we have,

$$v_m \approx V(r_0), \tag{3.32}$$

which means that the eigenvalues are approximately equal to the value of the central interaction potential at the radius r_0. Since any central interaction goes $\sim 1/r$, the eigenvalues v_m become much bigger as two particles close to each other (relative angular momentum m is decreasing).

One may generalize the Haldane pseudopotential to a many-body system. The interaction operator can be written in terms of the pseudopotential $v_{m'}$ as follows [2, 4, 9, 23],

$$V = \sum_{i<j} V(|z_i - z_j|) = \sum_{i<j} \sum_{m'=0} v_{m'} \mathcal{P}_{m'}(ij), \tag{3.33}$$

where $\mathcal{P}_{m'}(ij)$ is the projector operator that chooses electron pairs (i, j) that have relative angular momentum m'. We want to determine a unique Hamiltonian whose eigenstates are given by Laughlin wave functions (3.13). So, we need to get the desired Hamiltonian (3.33) by playing with Haldane-pseudopotential $v_{m'}$.

The Laughlin wave function (3.13) has (i, j) pairs that have relative angular momentum m due to the existence of the Vandermonde polynomial $(z_i - z_j)^m$. So, we can immediately notice that there are no pairs that have relative angular momentum m' which is less than m. So, one can allow for an extra energy cost for the $m' < m$ situation, while all others have zero energy cost:

$$v_{m'} = \begin{cases} 1, & \text{for} \quad m' < m \\ 0, & \text{for} \quad m' \geq m \end{cases} \tag{3.34}$$

As a result, Laughlin's wave function has zero energy for the short-range interaction since there is a finite energy cost when particles come closest to each other in Equation (3.32), which is already punished by the Haldane-pseudopotential (3.34).

CHAPTER 4

ROTATING BEC IN 2D PLANE

4.1 Introduction

The phenomenon of Bose–Einstein condensation (BEC) was first predicted by A. Einstein in 1924 [25]. Its experimental realization, achieved in dilute alkali gases such as sodium, rubidium-87, and lithium-7 [26–28], introduced a groundbreaking technique for cooling atomic gases. The particles that obey Bose statistics are represented by a one-particle wave function means that bosons occupy the same ground state below the critical temperature T_c, leading to a new state of matter called BEC [29]:

$$N_0(T) = N\left[1 - \left(\frac{T}{T_c}\right)^{\alpha}\right], \tag{4.1}$$

where $N_0(T)$ is the number of particles in the ground state, N is the total number of particles, T is tempeture, and α is constant that depends on the trap geometry. Also, the total number of particles is defined as follows, $N \equiv N_0 + N_{\text{ex}}$. In the equation (4.1), as temperature T is much smaller than the critical temperature T_c, then the number of particles in the excited states vanishes ($N_{\text{ex}} \to 0$), resulting in all particles occupying the ground state where the *Bose-Einstein Condensate* appears [30, 31].

Critical temperature T_c can be identified for various trap potentials. For instance, the value of $\alpha = 3$ represents the 3D anisotropic harmonic trap potential where the critical temperature is given by [29],

$$T_c^{(\alpha=3)} \approx 0.94\frac{\hbar}{k_B}(\omega_x\omega_y\omega_z N)^{1/3}, \tag{4.2}$$

where ω_i is the trap frequencies in the three direction $i = \{x, y, z\}$ and k_B is the Boltzmann constant. As an additional example, the value of $\alpha = 3/2$ represents the

3D box potential trap where the critical temperature is given by [29],

$$T_c^{(\alpha=3/2)} \approx 3.31 \frac{\hbar^2 n^{2/3}}{m k_B}, \tag{4.3}$$

where $n = N/V$ is the total number of particles per volume V and m is the mass of condensate.

While the Bose–Einstein condensate is often described by a single macroscopic wave function, which represents the macroscopic ground state degeneracy, real atomic species possess internal spin degrees of freedom arising from hyperfine interactions between the nuclear and electronic spins [29, 32, 33]. These internal states are particularly important in alkali atoms commonly used in BEC experiments.

The hyperfine interaction describes the coupling between between *nuclear* I and *electronic spins* J which can be described by the following model [29],

$$H_{\text{hf}} = A\boldsymbol{I} \cdot \boldsymbol{J}, \tag{4.4}$$

where A is hyperfine coupling constant, $\boldsymbol{I}$ and $\boldsymbol{J}$ are nuclear spin and electronic angular momentum (orbital + spin) operators, respectively. The total angular momentum is defined by,

$$\boldsymbol{F} = \boldsymbol{I} + \boldsymbol{J}, \tag{4.5}$$

Allowed values for total angular momentum:

$$F = \{|I - J|, |I - J| + 1, ..., I + J\}, \tag{4.6}$$

which is a usual rule for the addition of angular momentum. For instance, the electrons do not have orbital angular momentum L and have $S = 1/2$ electronic spin; therefore, electronic angular momentum equals $J = L + S = 1/2$. The nuclear spin I yields to two possible value of the total angular momentum F such that [29],

$$F = I \pm 1/2. \tag{4.7}$$

Most of the BEC experiments have been conducted by states having total electronic spin quantum number $S = 1/2$, and nuclear spin $I = 3/2$ (Rubidium-87, Sodium-23, Lithium-7). So, atoms that have been used in BEC experiments have multiple hyperfine F ground states [29]. In the experiments, the multiple hyperfine states of BEC are observed in optical trapped systems [32, 33].

In conclusion, hyperfine states that appear in BEC experiments play the role of internal degrees of freedom for the alkali atoms. That is why they can be used to create multi-component BECs (spinor BECs) [34–36] where different hyperfine spin states correspond to different species or components.

A particularly striking manifestation of BEC in both single- and multi-component condensates is the formation of quantized vortices under rotation [29, 37–41].

In certain simple cases, the behavior of condensed particles can be described using a nonlinear Schrödinger equation, commonly known as the Gross–Pitaevskii (GP) equation [42, 43]. This approach is primarily applicable under ultracold temperature conditions, making it especially suitable for experiments involving the alkali atoms typically used in Bose-Einstein condensation (BEC) experiments. The dynamics of the condensate (i.e., velocity) can be understood by the GP equation. The velocity of the condensate is calculated from the continuity equation, which is derived from the GP equations [29]:

$$\boldsymbol{v} = \frac{\hbar}{2mi}\frac{(\psi^*\nabla\psi - \psi\nabla\psi^*)}{|\psi|^2}, \tag{4.8}$$

where ψ is the single-particle condensate wave function that obeys the GP equation and m is the condensate mass. We assume that the condensate wave function takes the following form,

$$\psi(\boldsymbol{r}) = |\psi(\boldsymbol{r})|e^{i\phi(\boldsymbol{r})}. \tag{4.9}$$

Now, substitute the condensate wave function into the velocity expression (4.8). The gradient of the wave function:

$$\begin{aligned}\nabla\psi(\boldsymbol{r}) &= e^{i\phi(\boldsymbol{r})}(\nabla|\psi(\boldsymbol{r})| + i|\psi(\boldsymbol{r})|\nabla\phi(\boldsymbol{r}))\\ \nabla\psi(\boldsymbol{r})^* &= e^{-i\phi(\boldsymbol{r})}(\nabla|\psi(\boldsymbol{r})| - i|\psi(\boldsymbol{r})|\nabla\phi(\boldsymbol{r})).\end{aligned} \tag{4.10}$$

After substitution, we have [29, 37],

$$\boldsymbol{v} = \frac{\hbar}{m}\nabla\phi. \tag{4.11}$$

If ϕ is not a singular scalar, we say that the motion of the condensate must be irrotational, such that,

$$\nabla \times \boldsymbol{v} = 0, \tag{4.12}$$

where we used that the curl of the gradient of any scalar field is always the zero vector. The condensate wave function $\psi(\boldsymbol{r})$ is single valued; this is because the phase must

change by 2π or an integer multiple of 2π around a closed path C. We have,

$$\Delta\phi = \oint_C \nabla\phi \cdot d\boldsymbol{l} = 2\pi l, \tag{4.13}$$

where l is an integer. If we take the closed integral of the velocity:

$$\oint_C \boldsymbol{v} \cdot d\boldsymbol{l} = \frac{\hbar}{m}\Delta\phi = \frac{h}{m}l. \tag{4.14}$$

This demonstrates that a single-valued condensate wave function requires quantization in the units of h/m, which is called circulation [29, 37]. This circulation corresponds to the quantized vortices. The experimental evidence of quantum vortices verifies the rich physics in the rotation limits. The first quantized vortex was observed in rotating Helium-4 [38]. Additionally, multiple vortices were observed in rotating and trapped [39] and two-component BEC [40].

4.2 The Role of Superfluidity Under the Rotation

The liquid ^{4}He has unique responses to the rotation effect. The following analogy with the normal fluids can help to understand that the ^{4}He is crucial for rotating experimental setups [44]. Consider a hollow container filled with a normal fluid, such as water. Initially, the liquid is at rest. However, shortly after, it begins to move with the rotating container. When the container stops, the water gradually slows down and eventually comes to a stop due to the effects of viscosity.

Consider the same geometry again, but this time fill the hollow container with ^{4}He. Slowly begin to rotate the hollow. As you cool the ^{4}He below the critical temperature while the geometry continues to rotate, the liquid transitions into the superfluid state. Remarkably, the superfluid ^{4}He remains at rest in the laboratory frame despite the container's rotation. This phenomenon is known as the Hess-Fairbank effect [45], which highlights that the liquid remains at rest in the laboratory reference frame.

The interesting aspect of the experiment involves rapidly rotating ^{4}He. We follow the same procedure as discussed earlier, cooling down the hollow container while it is still spinning. The liquid begins to rotate with the container, even after it transitions into a superfluid state! If the container stops, the ^{4}He continues to rotate. This phenomenon indicates that the ^{4}He unique response to rotation.

Superfluidity in Helium-4 is a macroscopic quantum phenomenon that is a direct manifestation of Bose-Einstein condensation (BEC). Helium-4 atoms are bosons, and when cooled below the critical temperature $T_c = 2.17K$, a significant fraction of these atoms enter the same quantum ground state. This macroscopic occupation of a single quantum state is the essence of a BEC. That is why BEC experiments are important for rapidly rotating experiments [44].

4.3 Rotating Frame of Reference

Consider a two-dimensional BEC corresponding to the following Schrödinger equation in the presence of a time-dependent interaction potential $V(\boldsymbol{r}, t)$. We can express the Schrödinger equation in polar coordinates [46]:

$$i\hbar\frac{\partial\psi(\boldsymbol{r},\theta,t)}{\partial t} = \left[-\frac{\hbar^2}{2m}\left(\frac{1}{r}\frac{\partial}{\partial r}r\frac{\partial}{\partial r} + \frac{1}{r^2}\frac{\partial^2}{\partial\theta^2}\right) + V(\boldsymbol{r},\theta,t)\right]\psi(\boldsymbol{r},\theta,t), \tag{4.15}$$

We introduce a rigid body rotation in the z-direction with Ω frequency. The uniform rotational modification $\boldsymbol{\Omega} = \Omega\hat{z}$ can be described using the two degrees of freedom (t', θ') that are defined by,

$$\begin{aligned} t &\to t' \\ \theta &\to \theta' = \theta - \Omega t, \end{aligned} \tag{4.16}$$

where prime indices represent the new variables defined in the rotating frame of reference. Usage of the chain rule leads to the following transformations,

$$\begin{aligned} \frac{\partial}{\partial t} &= \frac{\partial}{\partial t'} - \Omega\frac{\partial}{\partial\theta'} \\ \frac{\partial}{\partial\theta} &= \frac{\partial}{\partial\theta'}. \end{aligned} \tag{4.17}$$

The angular momentum operator can be written in terms of the new degree of freedom θ' as follows,

$$L_z = (\boldsymbol{r}\times\boldsymbol{p})_z = -i\hbar\frac{\partial}{\partial\theta'}, \tag{4.18}$$

The left-hand side of the Scrödinger Equation (4.15) in the rotating frame of reference can be written in terms of the angular momentum operator:

$$i\hbar\frac{\partial\psi}{\partial t} \to i\hbar\left(\frac{\partial}{\partial t'} - \Omega\frac{\partial}{\partial\theta'}\right)\psi' = \left(i\hbar\frac{\partial}{\partial t'} + \Omega L_z\right)\psi', \tag{4.19}$$

The right-hand side of the Scrödinger Equation (4.15) remains unchanged because the kinetic term $\boldsymbol{p}^2/2m$ doesn't depend on the time, and partial derivation of the angular

part remains unchanged. Substituting the Equation (4.19) leads to the Schrödinger equation in the rotation frame of reference:

$$i\hbar\frac{\partial\psi(\boldsymbol{r},t')}{\partial t'} = \left[\frac{\boldsymbol{p}^2}{2m} - \Omega L_z + V(\boldsymbol{r},t')\right]\psi(\boldsymbol{r},t'), \tag{4.20}$$

where $\psi' = \psi(\boldsymbol{r},t')$. The more general single particle Hamiltonian in the rotating frame of reference can be written as,

$$H_\Omega = H_{\text{lab}} - \boldsymbol{\Omega}\cdot\boldsymbol{L}, \tag{4.21}$$

where $H_{\text{lab}} = \frac{\boldsymbol{p}^2}{2m} + V(\boldsymbol{r},t)$, $\boldsymbol{\Omega} = \Omega\hat{z}$ and, $\boldsymbol{L} = L_z\hat{z}$.

4.4 Eigenvalues

In this chapter, we cover the calculation of the eigenvalues of a rotating BEC with respect to the z-direction. Consider a 3D non-interacting N-body Hamiltonian that describes an electron system in a symmetric harmonic trap [37]:

$$H_{\text{lab}} = \sum_{i=1}^{N}\left[\frac{|\boldsymbol{p}_i|^2}{2m} + \frac{1}{2}m\omega_\perp^2(x_i^2+y_i^2) + \frac{1}{2}m\omega_\parallel^2 z_i^2\right], \tag{4.22}$$

where $\omega_\parallel$ and $\omega_\perp$ are the trap frequencies in the $x-y$ plane and $z-$direction, respectively. The single particle Hamiltonian in the rotating frame of reference can be calculated by using (4.21):

$$H_\Omega = \frac{p^2}{2m} + \frac{1}{2}m\omega_\perp^2(x^2+y^2) + \frac{1}{2}m\omega_\parallel^2 z^2 - \Omega(xp_y - yp_x), \tag{4.23}$$

where both the rotation frequency Ω and total angular momentum L have only z-direction. The z part of the Hamiltonian (4.23) is nothing but a dimensional harmonic oscillator with energies $E_{\Omega_z} = \hbar\omega_\parallel\left(n_\parallel + \frac{1}{2}\right)$, where $n_\parallel$ is an integer. The energy spectrum for the $x-y$ plane can be obtained by using creation and annihilation operators, which are defined as follows [44, 46],

$$a_\mu = \sqrt{\frac{m\omega_\perp}{2\hbar}}\left(\mu + i\frac{p_\mu}{m\omega_\perp}\right), \quad a_\mu^\dagger = \sqrt{\frac{m\omega_\perp}{2\hbar}}\left(\mu - i\frac{p_\mu}{m\omega_\perp}\right), \tag{4.24}$$

where $\mu = \{x,y\}$. After substitution, the $x-y$ plane of the Hamiltonian becomes:

$$H_{\Omega_{xy}} = \hbar\omega_\perp\left(a_x^\dagger a_x + a_y^\dagger a_y + 1\right) - i\hbar\Omega\left(a_y^\dagger a_x + a_x^\dagger a_y\right). \tag{4.25}$$

We have one more step to diagonalize the Hamiltonian fully. The new operator is defined as follows [44, 47, 48],

$$a_{\pm} = \frac{1}{\sqrt{2}}\left(a_x \mp i a_y\right), \quad a_{\pm}^{\dagger} = \frac{1}{\sqrt{2}}\left(a_x^{\dagger} \pm i a_y^{\dagger}\right), \tag{4.26}$$

where commutation relation obeys $[a_+, a_+^{\dagger}] = [a_-, a_-^{\dagger}] = 1$. The diagonalized Hamiltonian:

$$H_{\Omega_{xy}} = \hbar\omega_{\perp}\left(a_+^{\dagger}a_+ + a_-^{\dagger}a_- + 1\right) - \hbar\Omega\left(a_+^{\dagger}a_+ - a_-^{\dagger}a_-\right). \tag{4.27}$$

Since $[H_{\Omega_{xy}}, n_{\pm}] = 0$, where $n_{\pm} = a_{\pm}^{\dagger}a_{\pm}$, we can write the energy spectrum in the rotating frame of reference for the $x - y$ plane. We have,

$$E_{\Omega_{xy}} = \hbar\left[(\omega_{\perp} - \Omega)n_+ + (\omega_{\perp} + \Omega)n_- + \omega_{\perp}\right]. \tag{4.28}$$

We can write a more compact form by defining new quantum numbers [44]:

$$n \equiv n_+ + n_-, \quad m \equiv n_+ - n_-, \tag{4.29}$$

where n represents the LL index and m represents the angular momentum index. As a result, the eigenvalues can be found as follows,

$$E_{\Omega_{xy}} = n\hbar\omega_{\perp} - m\hbar\Omega + \hbar\omega_{\perp}. \tag{4.30}$$

There are three rotation limits in the 2D plane [44]. First is a non-rotating regime, meaning that the gas is stationary relative to the lab frame of reference. In this case, the eigenvalues are given by,

$$E_{\Omega=0} = \hbar\omega_{\perp}(n+1), \tag{4.31}$$

where eigenvalues have $n + 1$ degeneracy for each n level, resulting in the inverse pyramid form such that,

$$\begin{aligned} n = 0 &\Rightarrow m = 0 \\ n = 1 &\Rightarrow m = \pm 1 \\ n = 2 &\Rightarrow m = 0, \pm 2, \end{aligned} \tag{4.32}$$

where n_+ and n_- must be different from each other. The second limit is slowly-rotating, meaning the gas starts to rotate with $\Omega < \omega_{\perp}$. In this case, the eigenvalues if given by,

$$E_{\Omega<\omega_{\perp}} = \hbar\omega_{\perp}(n+1) - m\hbar\Omega, \tag{4.33}$$

where the eigenvalues are shifted by $m\hbar\Omega$ for the negative m values and by $-m\hbar\Omega$ for the positive m values. The last limit is called the rapidly rotating limit $\Omega \approx \omega_\perp$ in which the single-particle energy spectrum becomes LLs (2.17):

$$E_{\Omega\approx\omega_\perp} = 2\hbar\Omega\left(n_- + \frac{1}{2}\right), \tag{4.34}$$

where n_- serves a a LL index and they are spaced by $2\hbar\Omega$.

4.5 Rapidly Rotating BEC

In the previous chapter, we notice that the LL appears in the rapidly rotating limit $\Omega \approx \omega_\perp$. Now, we cover the bridge that connects rapidly rotating BEC and the IQHE model. The non-interacting single-particle Hamiltonian with a constant rotation frequency $\boldsymbol{\Omega} = \Omega\hat{z}$ in the rotation reference frame (4.23) can be modified in the following way,

$$H_\Omega = \frac{|\boldsymbol{p} - m(\boldsymbol{\Omega}\times\boldsymbol{r})|^2}{2m} + \frac{1}{2}m(x^2+y^2)(\omega_\perp^2 - \Omega^2) + \frac{1}{2}m\omega_\parallel^2 z^2, \tag{4.35}$$

where $r^2 = x^2 + y^2$. Consider 2D geometry $z = 0$ in the rapidly rotating limit ($\Omega \approx \omega_\perp$) the above Hamiltonian reduced to the following form,

$$H_\Omega = \frac{|\boldsymbol{p} - m(\boldsymbol{\Omega}\times\boldsymbol{r})|^2}{2m}, \tag{4.36}$$

which is the same as the IQHE model (2.14) that describes the motion of charged particles in a uniform magnetic field:

$$|\boldsymbol{p} - m(\boldsymbol{\Omega}\times\boldsymbol{r})|^2 = (\boldsymbol{p} + e\boldsymbol{A})^2. \tag{4.37}$$

We will end up with the following relation,

$$\boldsymbol{B}^* = \frac{2m}{e^*}\boldsymbol{\Omega}, \tag{4.38}$$

which means that the Coriolis effect (due to the rotation) plays the same role as the effective magnetic field $\boldsymbol{B^*}$ with quasi-charge e^*, even if there is no external magnetic field in the model.

The analogy between a rapidly rotating neutral gas (4.36) and a charged particle in a magnetic field (2.14) is exact only when the centrifugal force from rotation is balanced by the confining harmonic trap [37]. This balance occurs when the rotation

frequency approaches the transverse trap frequency $\Omega \approx \omega_\perp$. At exactly $\Omega = \omega_\perp$, the harmonic confinement in the $x - y$ plane is canceled by the centrifugal term, leaving only the Coriolis term that mimics the Lorentz force. If $\Omega > \omega_\perp$, the radial potential becomes negative (the middle term in the equation 4.35), leading to dynamical instability and loss of confinement. Therefore, stability requires $\Omega \leq \omega_\perp$ and this stability regime is called the 2D LLL [37], and the spectrum of the model (4.36) is given by LLs energies (4.34).

CHAPTER 5

BINARY BOSONIC GAS IN RAPIDLY ROTATING LIMIT

5.1 Introduction

The vortex's core size is determined by the healing length ξ [37]. When the healing length exceeds the inter-vortex spacing a_v, which can be tuned by adjusting the rotation frequency Ω, the BEC enters the strongly correlated regime. This regime is observed in the Rubidium condensate with a high rotation rate and low density [49]. High vortex density ($a_v << \xi$) refers to the situation where the number of vortices becomes comparable with the total number of particles, and strongly correlated phases can be understood with the FQHE states [4, 9, 50] such as the Laughlin wave function [19]. As discussed in previous chapters, studying the FQHE regime requires projection onto the LLL.

The weak interaction limit is crucial to allow the LLL approximation. The weak-interaction limit is achieved when the chemical potential $\mu \sim g\bar{n}$, where g is the interaction strength and $\bar{n}$ is the mean condensate density, is small compared to the energy gap, such that,

$$\mu << \hbar\omega_{\parallel}, 2\hbar\omega_{\perp}, \tag{5.1}$$

where $\hbar\omega_{\parallel}$ is the level spacing in the one-dimensional harmonic oscillator and $2\hbar\omega_{\perp}$ is the LLs spacing due to the rapid rotation of the BEC (4.34). Under these conditions ($a_v << \xi$ and μ is small compared to the single particle energy level gap), the single particle states are projected to the LLL.

5.2 Binary Bosonic Gas

In this section, we examine a two-component Bose gas that interacts through contact interaction in the rapidly rotating limit on a disc geometry. We employ the second quantization formalism, where the bosonic field operators $\Psi_\alpha(\boldsymbol{r})$ are expanded in this LLL basis (2.47). The many-body Hamiltonian in the second-quantized formalism for the contact interaction $V(|\boldsymbol{r}-\boldsymbol{r}'|) = g_{\alpha,\beta}\delta^2(\boldsymbol{r}-\boldsymbol{r}')$ is then given by,

$$H = \sum_{\alpha,\beta=1}^{2} \frac{g_{\alpha\beta}}{2} \int d\boldsymbol{r}^2 \Psi_\alpha^\dagger(\boldsymbol{r})\Psi_\beta^\dagger(\boldsymbol{r})\Psi_\beta(\boldsymbol{r})\Psi_\alpha(\boldsymbol{r}), \tag{5.2}$$

where $g_{\alpha,\beta}$ are the intra- and inter-species interaction strengths $g_{\alpha,\beta} = 4\pi\hbar^2 a_s^{(\alpha,\beta)}/M$, where M the mass of the condensate and $a_s^{(\alpha,\beta)}$ s-wave scattering length for bosonic species. We set $g_{11} = g_{22} = g = 1$ and $g_{12} = g_{21}$ to study in the units of coupling ratio g_{12}/g.

The field operator for species α can be written as $\Psi_\alpha(\boldsymbol{r}) = \sum_{m=0}^{M} \psi_m(z;\alpha)a_m(\alpha)$, where $\psi_m(z;\alpha)$ is the single particle LLL wave functions (2.47) for the α species, $a_m(\alpha)$ is the annihilation operator for a boson of species α in the LLL state with angular momentum m, and M is the maximum single-particle angular momentum. The Hamiltonian (5.2) can be written as,

$$\begin{aligned} H = & \sum_{m_1,m_2,m_3,m_4}^{M} V_{m_1,m_2,m_3,m_4} \frac{g_{11}}{2} \left(a_{m_1}^\dagger a_{m_2}^\dagger a_{m_3} a_{m_4}\right) \\ & + \frac{g_{22}}{2} \left(b_{m_1}^\dagger b_{m_2}^\dagger b_{m_3} b_{m_4}\right) \\ & + g_{12} \left(a_{m_1}^\dagger b_{m_2}^\dagger b_{m_3} a_{m_4}\right), \end{aligned} \tag{5.3}$$

where the matrix elements of the two-body operator are given by,

$$V_{m_1,m_2,m_3,m_4} = \int d^2\boldsymbol{r} d^2\boldsymbol{r}' \psi_{m_1}(z;\alpha)^* \psi_{m_2}(z;\beta)^* \delta^2(\boldsymbol{r}-\boldsymbol{r}')\psi_{m_3}(z;\alpha)\psi_{m_4}(z;\beta), \tag{5.4}$$

where we omit the $g_{\alpha,\beta}$ interaction term into the Hamiltonian (5.3). To calculate the matrix elements, we can use the polar coordinates (r,θ) and $z = re^{i\theta}$. The Dirac delta symbol can be written in cylindrical coordinates as,

$$\delta^{(2)}(\boldsymbol{r}-\boldsymbol{r'}) = \frac{1}{r}\delta(r-r')\delta(\theta-\theta'). \tag{5.5}$$

As a result, we have,

$$V_{m_1,m_2,m_3,m_4} = \frac{1}{2\pi l_B^2} \frac{(m_3+m_4)!}{2^{(m_3+m_4)}\sqrt{m_1!m_2!m_3!m_4!}} \delta_{m_1+m_2,m_3+m_4}, \tag{5.6}$$

where the total angular momentum in the $z-$direction L is conserved by the Kronecker delta term in the above expression, yielding a block diagonal Hamiltonian operator (5.3).

5.3 Numerical Analysis

In this sub-section, we provide exact diagonalization (ED) [51, 52] results up to $N = 5 + 5$ particles sector, whose Hilbert space dimension equals 147970 under the fixed total angular momentum $L = 45$ and finite Fock-space restricted by the integer angular momentum cut-off $M = 9$, meaning we can control the allowed values for the maximum single-particle angular momentum by changing the angular momentum cut-off M. The table (5.1) shows the Hilbert space dimensions for all parameter sets. The truncation of the single-particle basis to orbitals with angular momentum $m \leq M$ is necessary to create the many-body Hilbert space finite and thus computationally tractable.

We construct the two-component Hilbert space from the Fock basis. A many-body basis state is defined by specifying the occupation numbers of bosons of each species in the available single-particle angular momentum orbitals $m = 0, 1, 2.., M$, subject to the constraint that the total particle number for each species is fixed and the total angular momentum $L = \sum_{m=0}^{M} n_m m$, where n_m is the particle number occupied m angular momentum orbital, is conserved due to the axial symmetry in the model (4.22). Therefore, we construct the basis as follows,

$$\psi = |n_0, n_1, ..., n_m, ..., n_M\rangle \otimes |\tilde{n}_0, \tilde{n}_1, ..., \tilde{n}_m, ..., \tilde{n}_M\rangle \,, \tag{5.7}$$

where $(n, \tilde{n})$ represent the number of (α, β) bosonic species that occupy the corresponding orbitals, and the total number of particles is given by $N = \sum_{m=0}^{M} n_m + \sum_{m=0}^{M} \tilde{n}_m$.

N	M	L	$\mathcal{D}$
$2+2$	4	4	14
$3+3$	8	12	373
$3+3$	12	12	407
$4+4$	12	24	14120
$4+4$	24	24	16494
$5+5$	8	40	67095
$5+5$	9	35-45	97534-147970

Table 5.1: The Hilbert space dimensions $\mathcal{D}$ for the numeric parameters that we used in this thesis.

5.3.1 Energy Spectrum

The FQHE in the two-component bosonic gas is a well-studied problem in the literature [53–55]. On the other hand, rapidly rotating gas has been evaluated by using ED methods for spheres and torus geometries for searching candidates for an incompressible ground state, and the authors provide a ground state phase diagram as a function of coupling ratio g_{12}/g, including Laughlin's many-body wave function [56]. We study the Laughlin wave function as a function of negative coupling ratio $g_{12}/g \leq 0$ in the disc geometry, as well. Also, we investigate the instability region $g_{12}/g \lesssim -1$ [57].

We directly study two-component bosonic gas in the projected LLL subspace; however, the authors researched to check the validity of the LLL approximation for one-component rotating bosonic gases as a function of interaction strength [58].

First, we examine the Laughlin incompressible state ψ_{L} for a two-component system called the Laughlin square state $\Psi^2_{\text{Laughlin}} = \psi_{\mathrm{L}} \otimes \psi_{\mathrm{L}}$, which is the exact ground state with zero contact interaction energy for only repulsive coupling $g_{12}/g = 0$. The unnormalized many-body Laughlin square wave function can be easily generalized from the one-component Laughlin wave function (3.13). We have,

$$\Psi^2_{\text{Laughlin}} \propto \prod_{i<j} (z_i - z_j)^m (w_i - w_j)^m e^{-\sum_i (|z_i|^2 + |w_i|^2)/4l_B^2}, \tag{5.8}$$

where z, w are complex coordinates for the species and $\nu = 1/m$ are filling fractions for even angular momentum quantum numbers m. We study the one-half filling fraction $\nu = 1/2$ context in this thesis.

The Laughlin square state appears as $m(N-1) \leq M$, a condition is satisfied since the maximum single-particle angular momentum in the two-component Laughlin wave function (5.8) is $m(N-1)$. The total angular momentum is given by $L = 2\left(\frac{mN(N-1)}{2}\right)$, where 2 factor refers to the two component. Excitations of the Laughlin square states with a higher total angular momentum can contribute to the ground state, depending on the cut-off value M, i.e., one quasi-hole, center-of-mass, and edge states, etc [2, 4, 9, 59].

Energy spectrum as a function of total angular momentum L provides useful information about the incomprehensible states, especially the Laughlin wave function. The Laughlin wave function is observed for the one-component and rotating gas at the expected angular total momentum $L = mN(N-1)/2$ with its excitations [60, 61]. In this thesis, we diagonalize the Hamiltonian operator (5.3) to obtain the energy spectrum as a function of total angular momentum and, subsequently, verify the observation of the Laughlin square wave function.

In the Figure (5.1), we calculated the eigenvalues of the model (5.3) at the particle sector $N = 5 + 5$ and cut-off $M = 9$ with the coupling ratio $g_{12}/g = 0$. As a result, the ground state is degenerate and consists of the Laughlin squared state at $L = 40$ and its excitations, as expected.

5.3.2 Stability of Bosonic Mixtures

The spinor BEC becomes unstable in the negative strong coupling ratio $g_{12}/g << 0$, resulting in spatial collapse of the bosonic components [57, 62, 63]. The collapse phenomenon is widely observed in a one-component bosonic condensate [64, 65], Bose-Fermi mixtures changing inter-species interactions by Feshbach resonance [66, 67], and bosonic mixtures [68, 69].

We can write a stability condition for mixtures by following the mean-field energy expression of the model (5.2). In the mean-field approximation, the field operators

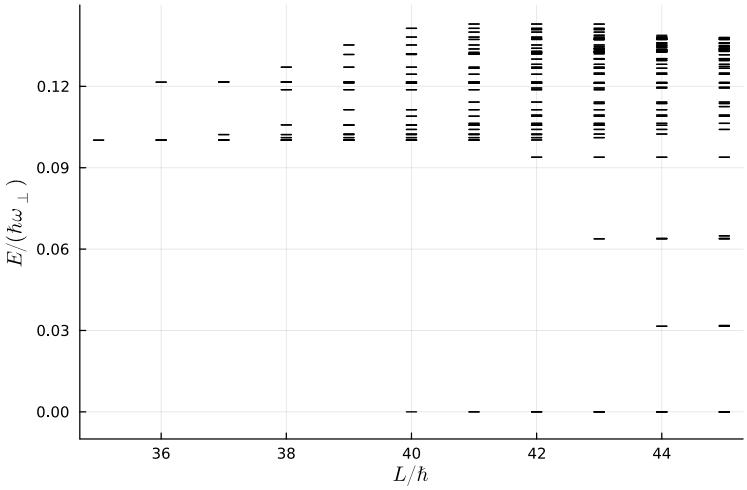

Figure 5.1: The low-lying energy E spectrum of the two-component rapidly rotating bosonic gas as a function of total angular momentum L in the range of $35 \leq L \leq 45$. The calculations are performed for a system of $N = 5 + 5$ particles with an angular momentum-cutoff of $M = 9$ and the coupling ratio is fixed at $g_{12}/g = 0$.

$\Psi_\alpha(\boldsymbol{r})$ are replaced by their expectation values, $\Psi_\alpha(\boldsymbol{r}) \to \langle\Psi_\alpha(\boldsymbol{r})\rangle = \psi_\alpha(\boldsymbol{r})$, meaning we can use the field operators as functions. From the Hamiltonian (5.2), one can read,

$$E = \frac{g_{11}}{2}|\psi_1(\boldsymbol{r})|^4 + \frac{g_{22}}{2}|\psi_2(\boldsymbol{r})|^4 + g_{12}|\psi_1(\boldsymbol{r})|^2|\psi_2(\boldsymbol{r})|^2, \tag{5.9}$$

which can also be written in the matrix notation:

$$E = \frac{1}{2}\begin{pmatrix} n_1 & n_2 \end{pmatrix}\begin{pmatrix} g_{11} & g_{12} \\ g_{12} & g_{22} \end{pmatrix}\begin{pmatrix} n_1 \\ n_2 \end{pmatrix}, \tag{5.10}$$

where $n_{1,2} = \psi^\dagger_{1,2}(\boldsymbol{r})\psi_{1,2}(\boldsymbol{r})$. The energy is positive definite, which requires simultaneously that $g_{11} > 0, g_{22} > 0$ and $\det\begin{pmatrix} g_{11} & g_{12} \\ g_{12} & g_{22} \end{pmatrix} > 0$. The positive determinant condition leads to a relation to stability:

$$g_{12}^2 < g_{11}g_{22}. \tag{5.11}$$

As a result, the multi-component gas can be stabilized as long as the $g_{12}^2 < g_{11}g_{22}$ condition is met; otherwise, the gas collapses. According to the parameter set that we use in this thesis, the critical coupling threshold value for the stability is given by,

$$g_{12}/g \sim -1. \tag{5.12}$$

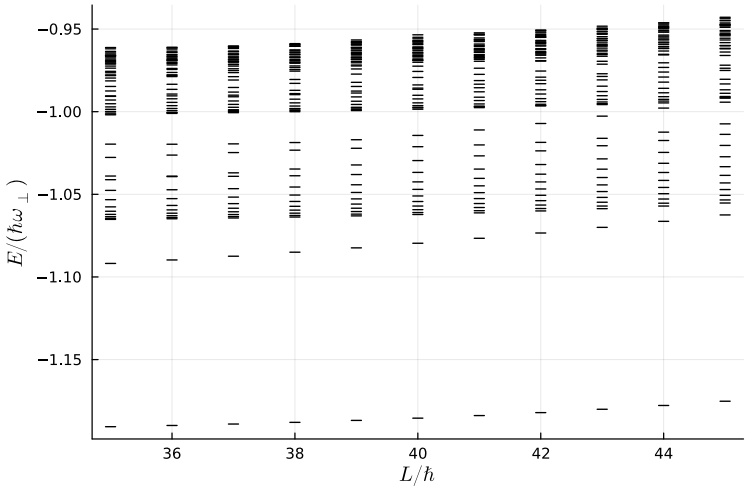

Figure 5.2: The low-lying energy E spectrum of the two-component rapidly rotating bosonic gas as a function of total angular momentum L in the range of $35 \leq L \leq 45$. The calculations are performed for a system of $N = 5 + 5$ particles with an angular momentum-cutoff of $M = 9$, and the coupling ratio is fixed at $g_{12}/g = -1.1$, which is below the threshold value.

The collapse condition (5.11) disrupts the positive definiteness of the energy expression (5.9), and in this case, we can define a unnormalized collapse state as follows,

$$\psi_{\text{Collapse}} \propto \left[\sum_{i=1}^{N}(z_i + w_i)\right]^{L}, \tag{5.13}$$

indicating that all complex coordinates of the bosons are in the common center of mass coordinate rotating with the same total angular momentum L, and a macroscopic occupation of the zero angular momentum state of the relative inter-species coordinate, leading to a spatial collapse of the two components onto each other. On the other hand, the possible maximum single particle angular momentum m should be equal to the total angular momentum L to describe the collapse state.

As the coupling ratio g_{12}/g becomes more attractive and crosses the critical threshold (5.12), a new, more energetically favorable configuration becomes available to the system. The Laughlin square state (5.8), which is designed to minimize repulsive intra-species energy by keeping particles apart, becomes a high-energy excited state. The system can drastically lower its total energy by forming a collapse state where the two species strongly overlap to maximize the attractive inter-species interaction.

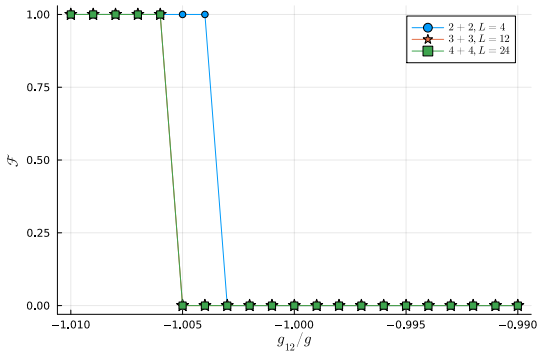

Figure 5.3: The overlap square $\mathcal{F}$ between the exact ground and analytic collapse state (5.13) as a funtion of coupling ratio g_{12}/g for three different particle sector: $N = \{2+2, 3+3\}$ and $N = 4+4$ are represented by blue circle, orange star and green square, respectively. To ensure that the basis is large enough to accurately describe the Laughlin square state and its potential transition to a collapse state, we use an angular momentum cutoff M equal to the total angular momentum of the Laughlin square state, $L = 2N(N-1)$, at filling fraction $\nu = 1/2$.

This transition is marked by the sharp drop in the ground state energy into negative values, as seen in the Figure (5.2).

5.3.2.1 Overlap Study

The overlap calculations are a standard tool to quantify how close a numerically obtained many-body state is to a trial or analytic state, such as the Laughlin and collapse wave function. For example, the authors verify that the Laughlin state appears roughly exactly ground state by using Density Matrix Renormalization Group (DMRG), which is a different technique from the ED calculations that we use in this thesis, on the sphere geometry [70]. In this thesis, as distinct from other research, we check the ground state (gs) characteristic for collapse analytic states by controlling the coupling ratio g_{12}/g with ED methods. First, we quantify the similarity between the numerically obtained ED ground state, $|\psi_{\text{ED}}\rangle$, and the analytic collapse ansatz (5.13), $|\psi_{\text{Collapse}}\rangle$, by computing the fidelity $\mathcal{F}$, which equals to overlap squared. It is defined as $\mathcal{F} = |\langle\psi_{\text{Collapse}}|\psi_{\text{ED}}\rangle|^2$. To compute this quantity, the analytical ansatz wave function must first be constructed numerically in the same many-body Fock

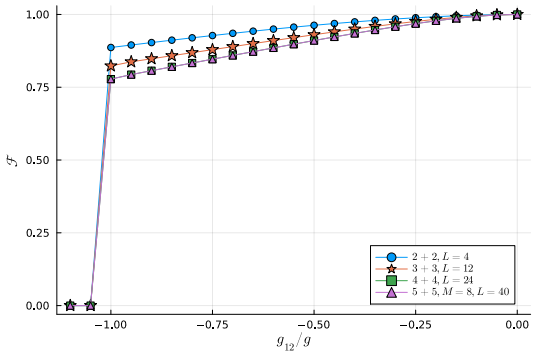

Figure 5.4: The overlap square $\mathcal{F}$ between the exact ground and analytic Laughlin square state (5.8) as a function of coupling ratio g_{12}/g for three different particle sector: $N = \{2+2, 3+3\}$ and $N = 4+4$ are represented by blue circle, orange star and green square, respectively. The data for the parameter set $N = 5+5, M = 8, L = 40$ is the same as the figure (5.1).

basis used for the exact diagonalization (5.7).

In the figure (5.3), we found that the collapse analytic wave function immediately occurs around the threshold value $g_{12}/g \sim -1$ by checking overlaps, which means that the stability condition (5.11) is consistent with our numerical result. We also obtained that the overlap value of the Laughlin square wave function begins at exactly identity (1) in the figure (5.4), and the data that is shown by purple upper triangle markers is consistent with our demonstration that the Laughlin square has zero ground state energy, as shown in Figure (5.1). The overlaps for the Laughlin square state decrease as the coupling ratio approaches the critical threshold $g_{12}/g \sim -1$, where the Laughlin state disappears in the ground state. It is worth noting that the overlap analysis for the $N = 5+5$ system is not presented, as the required angular momentum cutoff ($M = L = 40$) results in a Hilbert space dimension that is computationally intractable for our exact diagonalization method. However, the clear trend observed for systems up to $N = 4+4$ provides strong evidence for the transition between collapse and Laughlin square states in the figures (5.3, 5.4).

In conclusion, we observe that the sharp collapse transition at $g_{12}/g \sim -1$ is robust across a wide range of total angular momenta L. It is not surprising, since the collapse ansatz (5.13), by construction, is an eigenstate of the total angular momentum

operator with eigenvalue m. However, for sufficiently small total angular momentum L (e.g., $L = 6$ for $N = 4 + 4$), this clear transition observed in the overlap is smeared out or disappears, meaning we get identity overlap values between ground and collapse state in the region where coupling ratio is bigger than the critical threshold $-1 < g_{12}/g \lesssim 0$. This is a counterexample result. We do not know the reason for this.

5.3.2.2 Energy Gap Study

Incompressible quantum liquids, such as the Laughlin state, are defined by their resistance to density changes, resulting in uniform density (check Chapter III). This property arises because any local density perturbation requires the creation of fractionally charged excitations (quasiparticles and quasiholes, etc.). Crucially, creating such an excitation has a finite energy cost. A non-zero energy gap is therefore the fundamental signature of an incompressible state, as it ensures the stability and robustness of the ground state. Therefore, we can analyze the Laughlin square wave function by checking the gap between energy levels as a function of the coupling ratio g_{12}/g. We expect to see that since the Laughlin square wave function disappears after the critical threshold value (5.3) in the ground state, the signature of the gap must disappear as well.

Figure (5.5) provides clear evidence of a state transition driven by the inter-species interaction. For $g_{12}/g > -1$, the Laughlin square state is the gapped, incompressible ground state (blue line), and the first excited state is the collapse state (orange line). As g_{12}/g approaches the critical threshold $g_{12}/g \sim -1$, the energy of a competing state (the collapse state) decreases rapidly, causing the energy gap above the Laughlin state to close. At the critical threshold, the level crossing (level repulsion [71]) signifies that the gap has roughly vanished, and for $g_{12}/g \lesssim -1$, the system transitions into an unstable state where the collapse state becomes the ground state. Therefore, the closing of the energy gap, which is the defining feature of the incompressible Laughlin state, directly signals the destruction of this state and the emergence of the collapse mode in which the Laughlin square characteristic disappears. These observations are consistent with previous overlap calculations (5.3)

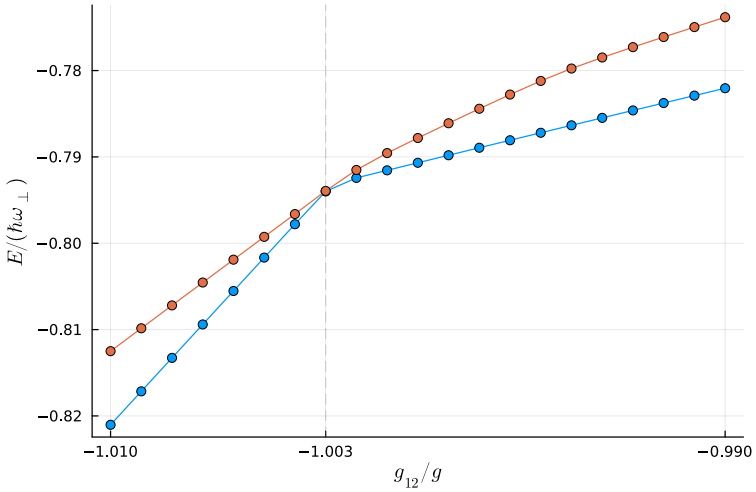

Figure 5.5: Eigenvalues of ground (blue line) and first excited (orange line) states as a function of coupling ratio g_{12}/g for $N = 5 + 5$ in the Laughlin square regime $M = 8, L = 40$. Level crossing occurs at the critical threshold value, indicated by a gray dashed vertical line at $g_{12}/g = -1.003$.

While for small systems ($N = 2 + 2$) the former Laughlin ground state becomes the new first excited state, we observe that this is not the case for larger particle sectors. For $N \geq 3 + 3$, the Laughlin square state is pushed much higher into the excited state manifold after the transition. We attribute this to a combination of the exponentially increasing many-body states and the resulting degeneracy in the excited state manifold. As g_{12}/g is tuned, the Laughlin state inevitably interacts with these nearby levels. According to the level repulsion, these interactions tend to push their energy upwards. Furthermore, its pure character dissolves into the complex manifold of excitations rather than surviving as a distinct, low-lying eigenstate. Therefore, the disappearance of the Laughlin state from the low-energy spectrum in larger systems is a natural consequence of the increasing complexity.

5.3.3 A Novel Ansatz: Molecular Laughlin

We propose an ansatz wave function describing the Laughlin regime's molecular formation for the bosonic particles. A strong inter-species attractive interaction g_{12} leads to molecular binding configurations in the collapse region $g_{12}/g \sim -1$, allowing us

to define a center of mass pair along inter-species bosons. Let us introduce an unnormalized many-body molecular ansatz as follows,

$$\Psi([z],[w]) \propto \sum_{\sigma \in S_N} \prod_{1 \leq i < j \leq N} \left(R_i^{(\sigma)} - R_j^{(\sigma)} \right)^4, \tag{5.14}$$

where $R_i^{(\sigma)} = z_i + w_{\sigma(i)}$ represents the center-of-mass between inter-species particles by the symmetric group S_N of degree total particle number N, which yields a fully symmetric wave function under the exchange of intra-species particles $z_i \leftrightarrow z_j, w_i \leftrightarrow w_j$. A Jastrow-like factor enforces repulsive correlations between molecules, resulting in molecular binding.

Interestingly, while the effective filling fraction is different ($\nu = 1/2$ for Laughlin square and $\nu' = 1/4$ for molecular ansatz), both the Laughlin square state and our molecular ansatz yield the same total angular momentum $L = 2N(N-1)$, making them direct competitors for the ground state within the same L sector. Also, the molecular ansatz appears in the angular momentum cut-off range $2m(N-1) \leq M$, which is two times the Laughlin square state. It is worth noting that we always study in the half-filling sector $\nu = 1/m = 1/2$.

In the figure (5.6), we provide the ground state overlap $\mathcal{F}$ as a function of g_{12}/g for the Laughlin square (5.8) and molecular ansatz (5.14). The ground state sharply drops the characteristic of the Laughlin square (blue lines) as close to the critical threshold $g_{12}/g \sim -1$, since the attractive inter-species interactions dominate the system. Our ansatz (red lines) becomes stronger in the same regime as the Laughlin square state, shifting the intersection points (black dots) to the collapse region. So that the molecular structure dominates the system until the gas collapses (5.13). The black cross symbols, in the Figure(5.6), mark the intersection points where the ground state has nearly equal overlap with both the Laughlin square and the molecular ansatz, signifying the center of the crossover region between the two competing descriptions.

Our results suggest a sequence of state transitions as g_{12}/g becomes more attractive: The system transitions from a standard Laughlin square into a molecular state, which dominates the ground state character in the $g_c < g_{12}/g < 0$ regime. This molecular state itself becomes unstable at the critical point $g_c \sim -1$, where the system undergoes a final transition into the spatially collapsed state (5.13)

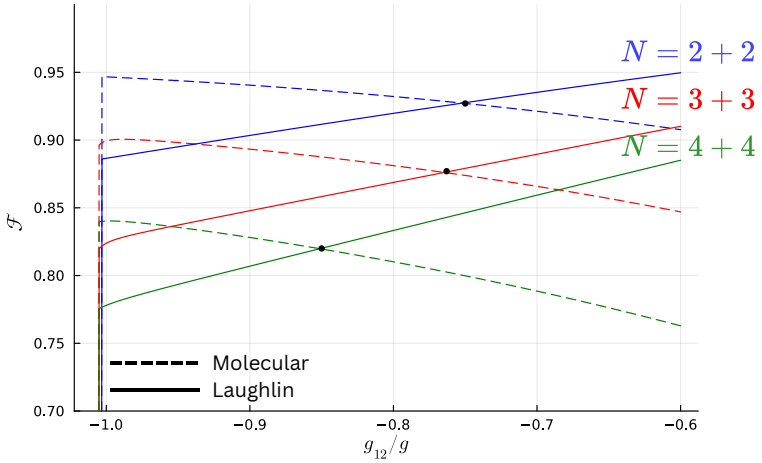

Figure 5.6: The ground state overlap $\mathcal{F}$ as a function of coupling ratio g_{12}/g for the Lauglin square (solid lines) and molecular ansatz (dashed lines) for the particle sectors $N = \{2+2, 3+3, 4+4\}$, blue, red, and green colors, respectively. The black dot symbols represent the intersection. The angular momentum cut-off is fixed by $M = 2m(N-1)$, where $m = 2$ for the one-half filling fraction Laughlin square.

5.3.4 Higher Excited States

Regardless of the type of wave function, any state, such as the Laughlin square or molecular ansatz, cannot exist in the ground state due to the presence of a collapse mode that occurs when $g_{12}/g \sim -1$. Therefore, we focus on the higher excited states, where the Laughlin square state (5.8) can persist.

We show that the non-zero ground state overlaps for the molecular ansatz that circulates between quasi-degenerate states in a specific energy window (Figure 5.7). We calculate the ground state overlaps as a function of eigenvalues to determine the special case where the quasi-degenerate band occurs. We can clearly see that the quasi-band is visible at $g_{12}/g = -1.027$ for $N = 4+4$ particle sector with $M = 12$ and $L = 24$ parameter set in the left panel of the Figure (5.7). In the same figure, we check the sorted eigenvalues (left panel) for a situation that consists of quasi-degeneracy, at $g_{12}/g = -1.027$. The relatively higher overlap values (red dots) are concentrated around the energy region (right panel), which is almost defined by the boundaries of the degenerate band.

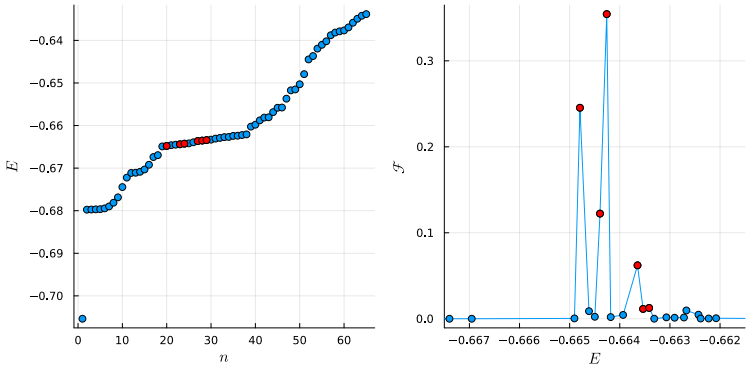

Figure 5.7: The sorted n eigenvalues E (left panel) and molecular ansatz overlap squares $\mathcal{F}$ as a function of eigenvalues (right panel) of the parameter space $N = 4{+}4$, $M = 12$ and $L = 24$. The red dots show the states that have relatively higher overlaps between $k = 65$ low-lying eigenstates. The coupling ratio is fixed at $g_{12}/g = -1.027$. The limits have been set for the x-axis on the right panel to show the quasi-degenerate band states.

In light of the above discussion, we introduce a concept called the sum of the overlap square:

$$\Lambda_k \equiv \sum_{i=1}^{k} \mathcal{F}_i, \tag{5.15}$$

where i shows the eigenstates indices and k is the upper limit for the number of low-lying eigenstates. As shown in the right panel of the figure (5.7), the sum of the overlap squares value (indicated by the red dots), which are relatively higher overlaps between $k = 65$ low-lying eigenstates, roughly equals $\Lambda_{k=65} \sim 0.82$. The molecular ansatz is written in terms of the ED states, where both of them are represented by the same occupation basis representations, resulting in $\Lambda_{k=\mathcal{D}} = 1$, where $\mathcal{D}$ is the Hilbert space dimension. So, we can interpret this result (5.7) in such a way that the molecular ansatz is predominantly a superposition of the quasi-degenerate states.

The molecular wave function spreads across quasi-degenerate states that must define the molecular ansatz. For this reason, we proposed a more robust way to determine the bandwidth of the quasi-degenerate stats. Bandwidth is defined as the energy difference between states on the quasi-degenerate band edges. The Figure (5.8) is obtained by starting from the midpoint of the quasi-degenerate band (left panel of the Figure 5.7) and proceeding by selecting a state from the right and one from the left at

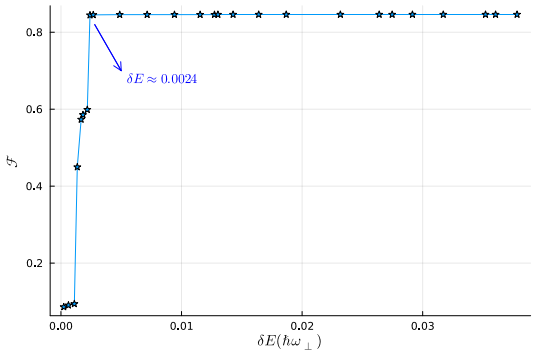

Figure 5.8: Molecular ansatz overlaps for the low-lying higher excited states as a function of bandwidth δE for the parameter set $N = 4 + 4, M = 12, L = 24$. We fixed the coupling ratio at $g_{12}/g = -1.027$.

each step, and summing their overlap square $\mathcal{F}$ as a function of δE which is a bandwidth for each steps. Given that the largest overlap contributions originate from this quasi-degenerate band, we see a convergence in the overlaps on the plot as soon as we capture this band. In this Figure (5.8), the first δE value after the jump in overlap provides an approximation of the band's width, which is roughly equal to $\delta E \approx 0.0024$. We identify the bandwidth of the quasi-degenerate with 4×10^{-4} error.

5.3.5 Real-Space Profile

Particle density operator $\hat{n}(\boldsymbol{r}) = \sum_a \delta(\boldsymbol{r} - \boldsymbol{r}_a)$ can be wirtten in terms of bosonic field operators $\Psi(\boldsymbol{r})$ in the second quantized formalism as follows,

$$\hat{n}(\boldsymbol{r}) = \Psi^\dagger(\boldsymbol{r})\Psi(\boldsymbol{r}), \tag{5.16}$$

The expectation value of the one-body density operator takes the following form,

$$\langle \hat{n}(z) \rangle = \sum_{m,n} \rho_{m,n} |\psi_m(z)|^2 \tag{5.17}$$

where $\psi_m(z)$ is the LLL wave function (2.47) in the symmetric gauge and $\rho_{m,n} = \langle \psi_n | a_m^\dagger a_m | \psi_n \rangle$ is the density operator such that $|\psi_n\rangle$ are exact diagonalization results and $(a^\dagger, a)$ bosonic creation/annihilation operators, respectively.

We evaluate the ground-state real-space one-species density in the Figure (5.9). The first column represents the density at the coupling $g_{12}/g = 0$, where the Laughlin

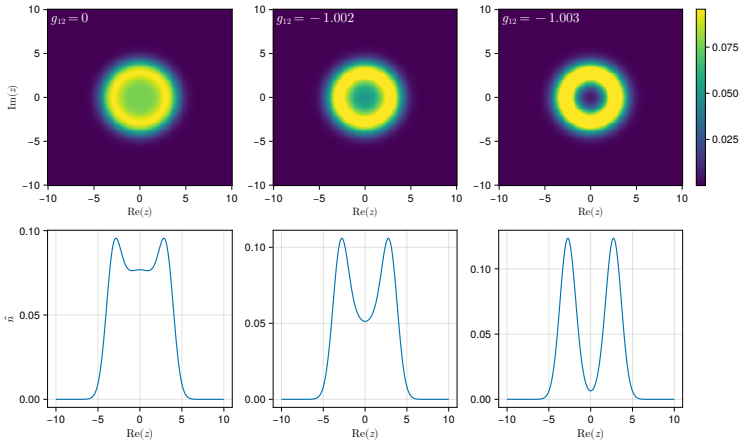

Figure 5.9: Real-space one species density of the ground state for attractive interaction $g_{12}/g = 0$, repulsive for the just before $g_{12}/g = -1.002$, and at the collapse critical threshold $g_{12}/g = -1.003$, respectively. The second row of the figure shows the one-dimensional cut of the first row, and the parameter set is $N = 5 + 5, M = 8, L = 40$.

square state (5.8) is the exact eigenstate of the model (5.2). From the LLL single particle wave functions (2.47), the radius of the Laughlin square state, where the density is peaked, is given by

$$R_{\text{peak}} = \sqrt{2m(N-1)l_B^2}, \tag{5.18}$$

where $m(N-1)$ is the highest possible single-particle relative angular momentum for the $\nu = 1/m$ filling fraction. Considering a uniform density $\rho = N/(\pi R_{peak}^2) = \nu/(2\pi l_B^2)$ where $\nu = 1/2$. As a result, the real-space density is roughly equal to the $\rho \approx 0.0795 l_B^2$. This result is very close to the central density in the leftmost column of the Figure (5.9), as expected. The density just before the collapse is calculated in the middle column at $g_{12} = -1.002$ in the same figure. The emergence of the ring-shaped density (rightmost column) of the collapse state (5.13) is a consequence of the conservation of the total angular momentum L. The exact total angular momentum of the Laughlin state is conserved by shifting the uniform density away from the origin. The plateau-like (quantum droplet) density (leftmost column) of the Laughlin state is transferred to the edge (rightmost column), where the collapse density is peaked since the total particle number N is also conserved.

CHAPTER 6

CONCLUSION

In Chapter 1, we reviewed the classical motion of an electron in a uniform magnetic field, which results in cyclotron orbits with cyclotron frequency ω_B. We then introduced the Drude model for the classical transport theory of electrons, which offers a more realistic picture than the single-electron cyclotron orbit model. From the Drude model, we reproduced the conductivity $\boldsymbol{\sigma}$ and resistivity $\boldsymbol{\rho}$ tensors that are key quantities for understanding the classical Hall effect. In particular, we demonstrated that the longitudinal resistivity ρ_{xx} and transverse (Hall) resistivity ρ_{xy} obtained from this framework successfully explain experimental results in the low-magnetic-field regime ($B \lesssim 1$).

Chapter 2 began with the classical equation of motion for charged particles in uniform magnetic and electric fields, leading to the Lorentz force. We then reviewed the quantization of energy levels into Landau levels (LLs) and solved the Schrödinger equation in both Landau and symmetric gauges. The symmetric gauge wave functions provided the lowest Landau level (LLL) eigenstates, which are essential for the fractional quantum Hall effect (FQHE) problem. We found that the eigenstates correspond to shifted eigenstates of a two-dimensional harmonic oscillator by $x_k = kl_B^2$. LLs are highly degenerate, and we demonstrated that the degeneracy equals the number of magnetic flux quanta N_Φ by calculating the uncertainty in the guiding center position. We also examined how an electric field lifts this degeneracy, yielding harmonic oscillator eigenstates shifted by $x_c = x_k + \frac{eE}{m\omega_B^2}$. Furthermore, we computed the expectation value of the quantum-mechanical current operator to explain the integer quantum Hall effect (IQHE). Using a confinement potential in the x-direction, we identified edge modes, enabling an interpretation of Hall quantization in terms

of insulating and conducting regions, linked to localized and extended states in the density of states. Finally, we discussed the effect of random impurity potentials and their relation to Hall quantization through the percolation picture.

In Chapter 3, we introduced the FQHE, where the Hall resistivity is quantized at fractional filling factors ν. We first solved the two-body problem in the LLL approximation, then extended the solution to many-body LLL wave functions for $\nu = 1$. We presented Laughlin's many-body wave function, describing the incompressible quantum droplet nature of FQHE states, and discussed its plasma analogy, which explains the droplet form through a uniform density attachment. We concluded with an overview of Haldane pseudopotentials, which provide the relevant energy scales for strongly interacting electrons.

Chapter 4 covered the fundamental concepts related to the later parts of the thesis, followed by an introduction to the rotating BEC model. We obtained the eigenvalue spectrum for various rotation limits and, in the final section, reviewed the rapidly rotating BEC model, which forms the foundation for Chapter 5.

In Chapter 5, we investigated a two-component bosonic gas in the LLL subspace on a disc geometry. We provided numerical evidence for several key findings. First, we identified the two-component Laughlin wave function within the zero-energy ground-state manifold, along with its excitations (center-of-mass and quasiparticles) for suitable parameter sets. Overlap calculations confirmed that the Laughlin wave function is the exact ground state at zero coupling ratio $g_{12}/g = 0$. For negative coupling ratios, we obtained the energy spectrum and observed that the ground state transitions to a collapse mode beyond a critical threshold $g_{12}/g \lesssim -1$. We analyzed the stability of the bosonic mixture, showing that the overlap results are consistent with our derived stability criterion, which is $g_{12}^2 < g_{11}g_{22}$. A study of the energy gap between the ground and first excited states revealed that the gap closes near the critical coupling ratio.

A central result of this thesis is the introduction of a novel ansatz for describing molecular structures via a Jastrow factor. We verified that the molecular overlaps increase as Laughlin overlaps decrease in the strongly attractive regime, up to the critical coupling ratio, indicating that molecular correlations dominate the system.

Furthermore, we demonstrated that the molecular wave function persists in higher excited states through quasi-degenerate energy bands, particularly near the post-critical regime, where these bands contribute significantly to the overlaps. We provided a refined method for determining the quasi-degenerate band width and identified it with high precision. Finally, we evaluated the real-space density profile of one species and examined its variation across different coupling ratio regimes.

Overall, this thesis bridges the theoretical frameworks of the integer and fractional quantum Hall effects with novel insights into the stability and collapse phenomena of two-component bosonic systems, offering a deeper understanding of strongly correlated states in the LLL subspace.

Bibliography

[1] E. H. Hall. "On a New Action of the Magnet on Electric Currents". In: *American Journal of Mathematics* 2.3 (1879), pp. 287–292. ISSN: 00029327, 10806377. URL: http://www.jstor.org/stable/2369245 (visited on 03/22/2025).

[2] M. O. Goerbig. *Quantum Hall Effects*. 2009. arXiv: 0909.1998 [cond-mat.mes-hall] URL: https://arxiv.org/abs/0909.1998.

[3] Charles Kittel and Paul Mceuen. *Introduction to solid state physics*. Wiley, 2018.

[4] Steven M. Girvin and Kun Yang. *Modern Condensed Matter Physics*. Cambridge University Press, 2019.

[5] P. Drude. "Zur Elektronentheorie der Metalle". In: *Annalen der Physik* 306.3 (1900), pp. 566–613. DOI: https://doi.org/10.1002/andp.19003060312. eprint: https://onlinelibrary.wiley.com/doi/pdf/10.1002/andp.19003060312. URL: https://onlinelibrary.wiley.com/doi/abs/10.1002/andp.19003060312.

[6] P. Drude. "Zur Elektronentheorie der Metalle; II. Teil. Galvanomagnetische und thermomagnetische Effecte". In: *Annalen der Physik* 308.11 (1900), pp. 369–402. DOI: https://doi.org/10.1002/andp.19003081102. eprint: https://onlinelibrary.wiley.com/doi/pdf/10.1002/andp.19003081102. URL: https://onlinelibrary.wiley.com/doi/abs/10.1002/andp.19003081102.

[7] S. M. Blinder. *Classical and Quantum Hall Effects*. Wolfram Demonstrations Project. 2020. URL: https://demonstrations.wolfram.com/ClassicalAndQuantumHallEffects/.

[8] "Solid State Physics. Von N. W. Ashcroft und N. D. Mermin; Holt, Rinehart and Winston, New York 1976, XXII, 826 Seiten, $19,95". In: *Physik in unserer Zeit* 9.1 (1978), pp. 33–33. DOI: https://doi.org/10.1002/

piuz.19780090109. eprint: https://onlinelibrary.wiley.com/doi/pdf/10.1002/piuz.19780090109. URL: https://onlinelibrary.wiley.com/doi/abs/10.1002/piuz.19780090109.

[9] David Tong. *Lectures on the Quantum Hall Effect*. 2016. arXiv: 1606.06687 [hep-th]. URL: https://arxiv.org/abs/1606.06687.

[10] Richard E. Prange and Steven M. Girvin. *The Quantum Hall effect*. Jan. 1990. DOI: 10.1007/978-1-4612-3350-3. URL: https://doi.org/10.1007/978-1-4612-3350-3.

[11] K. v. Klitzing, G. Dorda, and M. Pepper. "New Method for High-Accuracy Determination of the Fine-Structure Constant Based on Quantized Hall Resistance". In: *Phys. Rev. Lett.* 45 (6 Aug. 1980), pp. 494–497. DOI: 10.1103/PhysRevLett.45.494. URL: https://link.aps.org/doi/10.1103/PhysRevLett.45.494.

[12] Klaus von Klitzing. *Nobel lecture*. 2025. URL: https://www.nobelprize.org/prizes/physics/1985/klitzing/lecture/.

[13] Alba Cazorla. *Rhoxy*. Licensed under Creative Commons Attribution-ShareAlike 4.0 International (CC BY-SA 4.0). 2020. URL: https://commons.wikimedia.org/wiki/File:Rhoxy.jpg.

[14] Jainendra K. Jain. *Composite Fermions*. Cambridge University Press, 2007.

[15] Alexander Altland and Ben D. Simons. *Condensed Matter Field Theory*. 2nd ed. Cambridge University Press, 2010.

[16] Anton Akhmerov et al. *Topology in Condensed Matter — Syllabus*. 2025. URL: https://topocondmat.org/test/w3_pump_QHE-QHEedgestates.html.

[17] R. Willett et al. "Observation of an even-denominator quantum number in the fractional quantum Hall effect". In: *Phys. Rev. Lett.* 59 (15 Oct. 1987), pp. 1776–1779. DOI: 10.1103/PhysRevLett.59.1776. URL: https://link.aps.org/doi/10.1103/PhysRevLett.59.1776.

[18] R. Willett et al. "Observation of an even-denominator quantum number in the fractional quantum Hall effect". In: *Phys. Rev. Lett.* 59 (15 Oct. 1987),

pp. 1776–1779. DOI: 10.1103/PhysRevLett.59.1776. URL: https://link.aps.org/doi/10.1103/PhysRevLett.59.1776.

[19] R. B. Laughlin. “Anomalous Quantum Hall Effect: An Incompressible Quantum Fluid with Fractionally Charged Excitations”. In: *Phys. Rev. Lett.* 50 (18 May 1983), pp. 1395–1398. DOI: 10.1103/PhysRevLett.50.1395. URL: https://link.aps.org/doi/10.1103/PhysRevLett.50.1395.

[20] F. D. M. Haldane and E. H. Rezayi. “Finite-Size Studies of the Incompressible State of the Fractionally Quantized Hall Effect and its Excitations”. In: *Phys. Rev. Lett.* 54 (3 Jan. 1985), pp. 237–240. DOI: 10.1103/PhysRevLett.54.237. URL: https://link.aps.org/doi/10.1103/PhysRevLett.54.237.

[21] D. C. Tsui, H. L. Stormer, and A. C. Gossard. “Two-Dimensional Magnetotransport in the Extreme Quantum Limit”. In: *Phys. Rev. Lett.* 48 (22 May 1982), pp. 1559–1562. DOI: 10.1103/PhysRevLett.48.1559. URL: https://link.aps.org/doi/10.1103/PhysRevLett.48.1559.

[22] R. B. Laughlin. “Nobel Lecture: Fractional quantization”. In: *Rev. Mod. Phys.* 71 (4 July 1999), pp. 863–874. DOI: 10.1103/RevModPhys.71.863. URL: https://link.aps.org/doi/10.1103/RevModPhys.71.863.

[23] F. D. M. Haldane. “Fractional Quantization of the Hall Effect: A Hierarchy of Incompressible Quantum Fluid States”. In: *Phys. Rev. Lett.* 51 (7 Aug. 1983), pp. 605–608. DOI: 10.1103/PhysRevLett.51.605. URL: https://link.aps.org/doi/10.1103/PhysRevLett.51.605.

[24] D. S. Petrov, M. Holzmann, and G. V. Shlyapnikov. “Bose-Einstein Condensation in Quasi-2D Trapped Gases”. In: *Phys. Rev. Lett.* 84 (12 Mar. 2000), pp. 2551–2555. DOI: 10.1103/PhysRevLett.84.2551. URL: https://link.aps.org/doi/10.1103/PhysRevLett.84.2551.

[25] A. Einstein. “Quantentheorie des einatomigen idealen Gases”. In: *Albert Einstein: Akademie-Vorträge*. John Wiley Sons, Ltd, 2005, pp. 237–244. ISBN: 9783527608959. DOI: https://doi.org/10.1002/3527608958.

ch27. eprint: https://onlinelibrary.wiley.com/doi/pdf/10.1002/3527608958.ch27. URL: https://onlinelibrary.wiley.com/doi/abs/10.1002/3527608958.ch27.

[26] M. H. Anderson et al. "Observation of Bose-Einstein Condensation in a Dilute Atomic Vapor". In: *Science* 269.5221 (1995), pp. 198–201. DOI: 10.1126/science.269.5221.198. eprint: https://www.science.org/doi/pdf/10.1126/science.269.5221.198. URL: https://www.science.org/doi/abs/10.1126/science.269.5221.198.

[27] K. B. Davis et al. "Bose-Einstein Condensation in a Gas of Sodium Atoms". In: *Phys. Rev. Lett.* 75 (22 Nov. 1995), pp. 3969–3973. DOI: 10.1103/PhysRevLett.75.3969. URL: https://link.aps.org/doi/10.1103/PhysRevLett.75.3969.

[28] C. C. Bradley et al. "Evidence of Bose-Einstein Condensation in an Atomic Gas with Attractive Interactions". In: *Phys. Rev. Lett.* 75 (9 Aug. 1995), pp. 1687–1690. DOI: 10.1103/PhysRevLett.75.1687. URL: https://link.aps.org/doi/10.1103/PhysRevLett.75.1687.

[29] C. J. Pethick and H. Smith. *Bose–Einstein Condensation in Dilute Gases*. 2nd ed. Cambridge University Press, 2008.

[30] E. A. Cornell and C. E. Wieman. "Nobel Lecture: Bose-Einstein condensation in a dilute gas, the first 70 years and some recent experiments". In: *Rev. Mod. Phys.* 74 (3 Aug. 2002), pp. 875–893. DOI: 10.1103/RevModPhys.74.875. URL: https://link.aps.org/doi/10.1103/RevModPhys.74.875.

[31] Wolfgang Ketterle. "Nobel lecture: When atoms behave as waves: Bose-Einstein condensation and the atom laser". In: *Rev. Mod. Phys.* 74 (4 Nov. 2002), pp. 1131–1151. DOI: 10.1103/RevModPhys.74.1131. URL: https://link.aps.org/doi/10.1103/RevModPhys.74.1131.

[32] D. M. Stamper-Kurn et al. "Optical Confinement of a Bose-Einstein Condensate". In: *Phys. Rev. Lett.* 80 (10 Mar. 1998), pp. 2027–2030. DOI: 10.1103/PhysRevLett.80.2027. URL: https://link.aps.org/doi/10.1103/PhysRevLett.80.2027.

[33] W. Ketterle, D. S. Durfee, and D. M. Stamper-Kurn. *Making, probing and understanding Bose-Einstein condensates*. 1999. arXiv: cond-mat/9904034 [cond-mat]. URL: https://arxiv.org/abs/cond-mat/9904034.

[34] Masahito Ueda. "Spinor Bose-Einstein condensates". In: *Contemporary Physics* 63.2 (2022), pp. 106–115. DOI: 10.1080/00107514.2023.2172817. eprint: https://doi.org/10.1080/00107514.2023.2172817. URL: https://doi.org/10.1080/00107514.2023.2172817.

[35] Tin-Lun Ho. "Spinor Bose Condensates in Optical Traps". In: *Phys. Rev. Lett.* 81 (4 July 1998), pp. 742–745. DOI: 10.1103/PhysRevLett.81.742. URL: https://link.aps.org/doi/10.1103/PhysRevLett.81.742.

[36] Tin-Lun Ho and V. B. Shenoy. "Binary Mixtures of Bose Condensates of Alkali Atoms". In: *Phys. Rev. Lett.* 77 (16 Oct. 1996), pp. 3276–3279. DOI: 10.1103/PhysRevLett.77.3276. URL: https://link.aps.org/doi/10.1103/PhysRevLett.77.3276.

[37] N.R. Cooper. "Rapidly rotating atomic gases". In: *Advances in Physics* 57.6 (2008), pp. 539–616. DOI: 10.1080/00018730802564122. eprint: https://doi.org/10.1080/00018730802564122. URL: https://doi.org/10.1080/00018730802564122.

[38] Russell J Donnelly. *Quantized vortices in helium II*. Vol. 2. Cambridge University Press, 1991.

[39] K. W. Madison et al. "Vortex Formation in a Stirred Bose-Einstein Condensate". In: *Phys. Rev. Lett.* 84 (5 Jan. 2000), pp. 806–809. DOI: 10.1103/PhysRevLett.84.806. URL: https://link.aps.org/doi/10.1103/PhysRevLett.84.806.

[40] M. R. Matthews et al. "Vortices in a Bose-Einstein Condensate". In: *Phys. Rev. Lett.* 83 (13 Sept. 1999), pp. 2498–2501. DOI: 10.1103/PhysRevLett.83.2498. URL: https://link.aps.org/doi/10.1103/PhysRevLett.83.2498.

[41] Lev Pitaevskii and Sandro Stringari. *Bose-Einstein Condensation and Superfluidity*. Oxford University Press, Jan. 2016. ISBN: 9780198758884. DOI: 10.

1093/acprof:oso/9780198758884.001.0001. URL: https://doi.org/10.1093/acprof:oso/9780198758884.001.0001.

[42] E. P. Gross. "Structure of a quantized vortex in boson systems". In: *Il Nuovo Cimento* 20.3 (May 1961), pp. 454–477. DOI: 10.1007/bf02731494.

[43] Lev Petrovich Pitaevskii. "Vortex Lines in an Imperfect Bose Gas". In: *Sov. Phys. JETP.* 13.2 (Aug. 1961), p. 451.

[44] Anthony J. Leggett. "Bose-Einstein condensation in the alkali gases: Some fundamental concepts". In: *Rev. Mod. Phys.* 73 (2 Apr. 2001), pp. 307–356. DOI: 10.1103/RevModPhys.73.307. URL: https://link.aps.org/doi/10.1103/RevModPhys.73.307.

[45] G. B. Hess and W. M. Fairbank. "Measurements of Angular Momentum in Superfluid Helium". In: *Phys. Rev. Lett.* 19 (5 July 1967), pp. 216–218. DOI: 10.1103/PhysRevLett.19.216. URL: https://link.aps.org/doi/10.1103/PhysRevLett.19.216.

[46] Takumi Yoshino. "Theoretical Study of Binary Bose-Einstein Condensates under Synthetic Gauge Fields". PhD thesis. Department of Physics, Graduate School of Science, The University of Tokyo, 2020.

[47] Albert Messiah. *Quantum Mechanics Vol I*. New york: Wiley, 1961.

[48] Claude Cohen-Tannoudji and Franck Laloë Bernard Diu. *Quantum Mechanics*. New york, 1977.

[49] M. Cozzini, S. Stringari, and C. Tozzo. "Vortex lattices in Bose-Einstein condensates: From the Thomas-Fermi regime to the lowest-Landau-level regime". In: *Phys. Rev. A* 73 (2 Feb. 2006), p. 023615. DOI: 10.1103/PhysRevA.73.023615. URL: https://link.aps.org/doi/10.1103/PhysRevA.73.023615.

[50] Sankar Das Sarma and Aron Pinczuk. *Perspectives in Quantum Hall Effects: Novel quantum liquids in low-dimensional semiconductor structures*. Wiley VCH, 2008.

[51] Alexander Weiße and Holger Fehske. "Exact Diagonalization Techniques". In: *Computational Many-Particle Physics*. Ed. by H. Fehske, R. Schneider, and A. Weiße. Berlin, Heidelberg: Springer Berlin Heidelberg, 2008, pp. 529–544.

ISBN: 978-3-540-74686-7. DOI: 10.1007/978-3-540-74686-7_18. URL: https://doi.org/10.1007/978-3-540-74686-7_18.

[52] Cornelius Lanczos. "An iteration method for the solution of the eigenvalue problem of linear differential and integral operators". In: *Journal of Research of the National Bureau of Standards* 45.4 (Oct. 1950). DOI: 10.6028/jres.045.026. URL: https://hal.science/hal-01712947.

[53] T. Graß et al. "Quantum Hall phases of two-component bosons". In: *Phys. Rev. B* 89 (4 Jan. 2014), p. 045114. DOI: 10.1103/PhysRevB.89.045114. URL: https://link.aps.org/doi/10.1103/PhysRevB.89.045114.

[54] Shunsuke Furukawa and Masahito Ueda. "Integer Quantum Hall State in Two-Component Bose Gases in a Synthetic Magnetic Field". In: *Phys. Rev. Lett.* 111 (9 Aug. 2013), p. 090401. DOI: 10.1103/PhysRevLett.111.090401. URL: https://link.aps.org/doi/10.1103/PhysRevLett.111.090401.

[55] Ying-Hai Wu and Jainendra K. Jain. "Quantum Hall effect of two-component bosons at fractional and integral fillings". In: *Phys. Rev. B* 87 (24 June 2013), p. 245123. DOI: 10.1103/PhysRevB.87.245123. URL: https://link.aps.org/doi/10.1103/PhysRevB.87.245123.

[56] Shunsuke Furukawa and Masahito Ueda. "Quantum Hall phase diagram of two-component Bose gases: Intercomponent entanglement and pseudopotentials". In: *Phys. Rev. A* 96 (5 Nov. 2017), p. 053626. DOI: 10.1103/PhysRevA.96.053626. URL: https://link.aps.org/doi/10.1103/PhysRevA.96.053626.

[57] D. S. Petrov. "Quantum Mechanical Stabilization of a Collapsing Bose-Bose Mixture". In: *Phys. Rev. Lett.* 115 (15 Oct. 2015), p. 155302. DOI: 10.1103/PhysRevLett.115.155302. URL: https://link.aps.org/doi/10.1103/PhysRevLett.115.155302.

[58] Alexis G. Morris and David L. Feder. "Validity of the lowest-Landau-level approximation for rotating Bose gases". In: *Phys. Rev. A* 74 (3 Sept. 2006), p. 033605. DOI: 10.1103/PhysRevA.74.033605. URL: https://link.aps.org/doi/10.1103/PhysRevA.74.033605.

[59] Martin Greiter and Frank Wilczek. *Fractional Statistics*. 2022. arXiv: 2210.02530 [cond-mat.str-el]. URL: https://arxiv.org/abs/2210.02530.

[60] S. Viefers, T. H. Hansson, and S. M. Reimann. "Bose condensates at high angular momenta". In: *Phys. Rev. A* 62 (5 Oct. 2000), p. 053604. DOI: 10.1103/PhysRevA.62.053604. URL: https://link.aps.org/doi/10.1103/PhysRevA.62.053604.

[61] N Regnault et al. "Composite fermion theory of rapidly rotating two-dimensional bosons". In: *Journal of Physics B Atomic Molecular and Optical Physics* 39.10 (May 2006), S89–S99. DOI: 10.1088/0953-4075/39/10/s09. URL: https://doi.org/10.1088/0953-4075/39/10/s09.

[62] G. K. Chaudhary and R. Ramakumar. "Collapse dynamics of a ^{176}Yb-^{174}Yb Bose-Einstein condensate". In: *Phys. Rev. A* 81 (6 June 2010), p. 063603. DOI: 10.1103/PhysRevA.81.063603. URL: https://link.aps.org/doi/10.1103/PhysRevA.81.063603.

[63] Cosetta Baroni, Giacomo Lamporesi, and Matteo Zaccanti. "Quantum mixtures of ultracold gases of neutral atoms". In: *Nature Reviews Physics* 6.12 (Dec. 2024), pp. 736–752. ISSN: 2522-5820. DOI: 10.1038/s42254-024-00773-6. URL: https://doi.org/10.1038/s42254-024-00773-6.

[64] Elizabeth A. Donley et al. "Dynamics of collapsing and exploding Bose–Einstein condensates". In: *Nature* 412.6844 (July 2001), pp. 295–299. ISSN: 1476-4687. DOI: 10.1038/35085500. URL: https://doi.org/10.1038/35085500.

[65] Christoph Eigen et al. "Observation of Weak Collapse in a Bose-Einstein Condensate". In: *Phys. Rev. X* 6 (4 Dec. 2016), p. 041058. DOI: 10.1103/PhysRevX.6.041058. URL: https://link.aps.org/doi/10.1103/PhysRevX.6.041058.

[66] S. Ospelkaus et al. "Tuning of Heteronuclear Interactions in a Degenerate Fermi-Bose Mixture". In: *Phys. Rev. Lett.* 97 (12 Sept. 2006), p. 120403. DOI: 10.1103/PhysRevLett.97.120403. URL: https://link.aps.org/doi/10.1103/PhysRevLett.97.120403.

[67] C. Ospelkaus et al. “Interaction-Driven Dynamics of $^{40}\mathrm{K}-^{87}\mathrm{Rb}$ Fermion-Boson Gas Mixtures in the Large-Particle-Number Limit”. In: *Phys. Rev. Lett.* 96 (2 Jan. 2006), p. 020401. DOI: 10.1103/PhysRevLett.96.020401. URL: https://link.aps.org/doi/10.1103/PhysRevLett.96.020401.

[68] C. R. Cabrera et al. “Quantum liquid droplets in a mixture of Bose-Einstein condensates”. In: *Science* 359.6373 (2018), pp. 301–304. DOI: 10.1126/science.aao5686. eprint: https://www.science.org/doi/pdf/10.1126/science.aao5686. URL: https://www.science.org/doi/abs/10.1126/science.aao5686.

[69] G. Semeghini et al. “Self-Bound Quantum Droplets of Atomic Mixtures in Free Space”. In: *Phys. Rev. Lett.* 120 (23 June 2018), p. 235301. DOI: 10.1103/PhysRevLett.120.235301. URL: https://link.aps.org/doi/10.1103/PhysRevLett.120.235301.

[70] A. E. Feiguin et al. “Density Matrix Renormalization Group Study of Incompressible Fractional Quantum Hall States”. In: *Phys. Rev. Lett.* 100 (16 Apr. 2008), p. 166803. DOI: 10.1103/PhysRevLett.100.166803. URL: https://link.aps.org/doi/10.1103/PhysRevLett.100.166803.

[71] J. J. Sakurai and Jim Napolitano. *Modern Quantum Mechanics*. 3rd ed. Cambridge University Press, 2020.